The FEBS Journal

FEBS PRESS
science publishing by scientists

Substrate specificity and complex stability of coproporphyrin ferrochelatase is governed by hydrogen-bonding interactions of the four propionate groups

Thomas Gabler[1], Federico Sebastiani[2], Johannes Helm[1], Andrea Dali[2], Christian Obinger[1], Paul G. Furtmüller[1], Giulietta Smulevich[2,3] and Stefan Hofbauer[1]

1 Department of Chemistry, Institute of Biochemistry, University of Natural Resources and Life Sciences, Vienna, Austria
2 Dipartimento di Chimica 'Ugo Schiff' (DICUS), Università di Firenze, Sesto Fiorentino, Italy
3 INSTM Research Unit of Firenze, Sesto Fiorentino, Italy

Keywords
enzyme kinetics; ferrochelatase; haeme biosynthesis; resonance Raman; site-directed mutagenesis

Correspondence
S. Hofbauer, Department of Chemistry, Institute of Biochemistry, University of Natural Resources and Life Sciences, Vienna, Muthgasse 18, A-1190 Vienna, Austria
Tel: +43 1 47654 77258
E-mail: stefan.hofbauer@boku.ac.at
and
G. Smulevich, Dipartimento di Chimica 'Ugo Schiff' (DICUS), Università di Firenze, Via della Lastruccia 3-13, I-50019 Sesto Fiorentino (FI), Italy
Tel: +39 055 4573083
E-mail: giulietta.smulevich@unifi.it

(Received 10 September 2021, revised 19 October 2021, accepted 28 October 2021)

doi:10.1111/febs.16257

Coproporpyhrin III is the substrate of coproporphyrin ferrochelatases (CpfCs). These enzymes catalyse the insertion of ferrous iron into the porphyrin ring. This is the penultimate step within the coproporphyrin-dependent haeme biosynthesis pathway. This pathway was discovered in 2015 and is mainly utilised by monoderm bacteria. Prior to this discovery, monoderm bacteria were believed to utilise the protoporphyrin-dependent pathway, analogously to diderm bacteria, where the substrate for the respective ferrochelatase is protoporphyrin IX, which has two propionate groups at positions 6 and 7 and two vinyl groups at positions 2 and 4. In this work, we describe for the first time the interactions of the four-propionate substrate, coproporphyrin III, and the four-propionate product, iron coproporphyrin III (coproheme), with the CpfC from *Listeria monocytogenes* and pin down differences with respect to the protoporphyrin IX and haeme *b* complexes in the wild-type (WT) enzyme. We further created seven *Lm*CpfC variants aiming at altering substrate and product coordination. The WT enzyme and all the variants were comparatively studied by spectroscopic, thermodynamic and kinetic means to investigate in detail the H-bonding interactions, which govern complex stability and substrate specificity. We identified a tyrosine residue (Y124 in *Lm*CpfC), coordinating the propionate at position 2, which is conserved in monoderm CpfCs, to be highly important for binding and stabilisation. Importantly, we also describe a tyrosine-serine-threonine triad, which coordinates the propionate at position 4. The study of the triad variants indicates structural differences between the coproporphyrin III and the coproheme complexes.

Enzyme
EC 4.99.1.9

Abbreviations
5c, 5-coordinated; 6c, 6-coordinated; *Bs*, *Bacillus subtilis*; CgoX, coproporphyrinogen oxidase; ChdC, coproheme decarboxylase; coproheme, iron coproproporphyrin III; CPD, coproporphyrin-dependent; CpfC, coproporphyrin ferrochelatase; cpIII, coproporphyrin III; cw, continuous-wave; DSC, differential scanning calorimetry; dSDP, 2,4-disulfonic acid deuteroporphyrin IX; HPLC, high performance liquid chromatography; HS, high-spin; *Lm*, *Listeria monocytogenes*; MALS, multi angle light scattering; NMMP, *N*-methylmesoporphyrin; PgoX, protoporphyrinogen oxidase; PPD, protoporphyrin-dependent; PpfC, protoporphyrin ferrochelatase; ppIX, protoporphyrin IX; RR, resonance Raman; *Sa*, *Staphylococcus aureus*; SEC, size exclusion chromatography; WT, wild-type.

Introduction

Ferrochelatases insert ferrous iron into tetrapyrrole macrocycles [1,2]. In the prokaryotic world, ferrochelatases are essential for haeme *b* biosynthesis [3]. In the ‘protoporphyrin-dependent’ (PPD) haeme biosynthesis pathway the protoporphyrin ferrochelatase (PpfC) is active, whereas in the ‘coproporphyrin-dependent’ (CPD) haeme biosynthesis pathway, coproporphyrin ferrochelatase (CpfC) is present (comprehensive figures of an overview of the pathways can be found in Refs [3–6]). Diderm bacteria predominantly utilise the PPD pathway, whereas monoderm bacteria utilise the CPD pathway (Fig. 1) [3,6], which was identified in 2015 and opened a new chapter in the process of understanding prokaryotic haeme biosynthesis [7]. The names of these enzymes already specify their substrates (protoporphyrin IX and coproporphyrin III, respectively) [3]. Coproporphyrin III differs from protoporphyrin IX in having propionate groups at positions 2 and 4 of the pyrrole ring instead of vinyl groups. Both pathways yield the same final product, haeme *b*, which is an essential iron-containing co-factor for almost all living organisms [8]. In the PPD pathway PpfC catalyzes the formation of haeme *b* in the final step. In the CPD pathway, CpfC produces iron coproporphyrin III (coproheme), which is the substrate for coproheme decarboxylase (ChdC). ChdCs catalyse the ultimate reaction in the CPD pathway, in which propionate groups at positions 2 and 4 of coproheme are decarboxylated to vinyl groups under concomitant release of CO_2 [4,9,10].

At a first glimpse, prokaryotic PpfC and CpfC structures appear to be highly similar. They are monomeric enzymes (in contrast to dimeric human PpfC) and share the same subunit architecture, which consists of two ferredoxin-like folds [3,5,11]. Within the monoderm representatives, significant differences are observed in the sequence length of CpfCs between Actinobacteria and Firmicutes. Actinobacterial CpfCs are longer and have a C-terminal [2Fe-2S] cluster of yet unknown function. As a side note, it is worth mentioning that the dimeric human ferrochelatase is also an iron-sulfur protein, but analogously, the role of this cofactor is still undiscovered [12,13].

Studies prior to 2015 on CpfCs were performed without the knowledge of the CPD pathway, and therefore used protoporphyrin IX as the substrate for biochemical, biophysical and structural investigations. These investigations were mainly performed on the ferrochelatase of firmicute *Bacillus subtilis* [14–17]. Thereafter, some studies report biochemical data with the correct substrate on CpfC from *Staphylococcus aureus* [18–21]. Recently, we solved the first coproheme-bound structure of the CpfC from the firmicute *Listeria monocytogenes* (*Lm*CpfC) [5], and we identified a

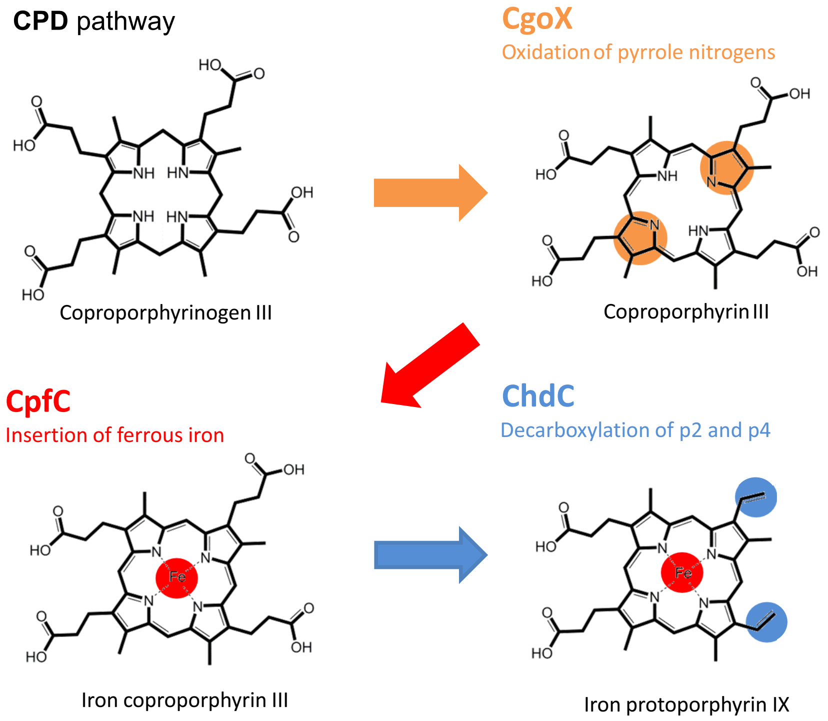

Fig. 1. Overview of the CPD haeme biosynthesis pathway starting from coproporphyrinogen III.

high degree of non-covalent interactions between coproheme propionate groups and the protein moiety (Fig. 2A, structural overview). These interactions are targeting amino acid residues, which are conserved within Firmicutes (Y12, T14, R29; *Lm*CpfC numbering) and for some positions also conserved within all the sampled monoderm representatives (Y124, *Lm*CpfC numbering). Y46 and S53 (*Lm*CpfC

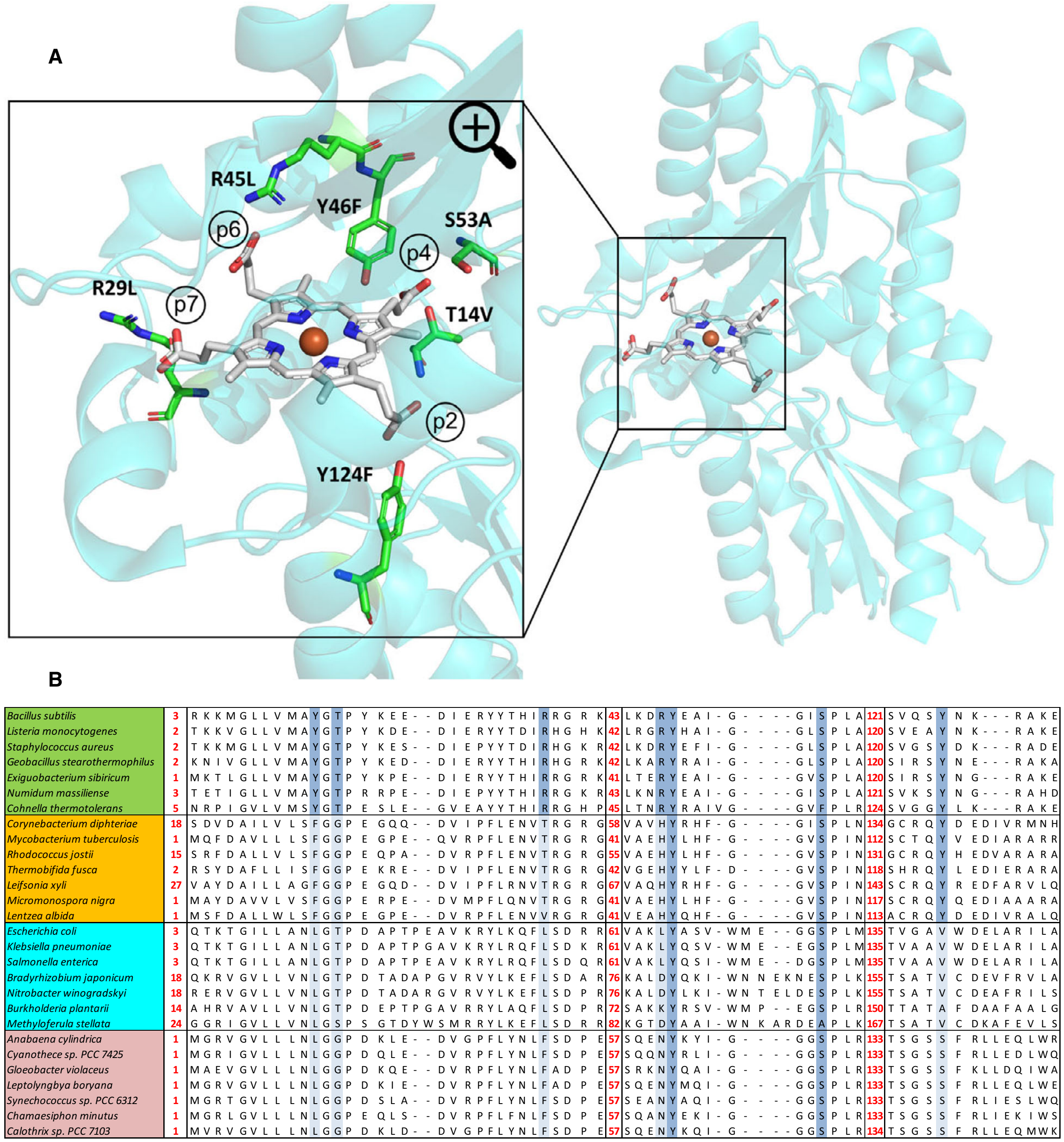

Bacillus subtilis	3	RKKMGLLVMAYGTPYKEE--DIERYYTHIRRGRK	43	LKDRYEAI-G----GISPLA	121	SVQSYNK---RAKE
Listeria monocytogenes	2	TKKVGLLVMAYGTPYKDE--DIERYYTDIRHGHK	42	LRGRYHAI-G----GLSPLA	120	SVEAYNK---RAKE
Staphylococcus aureus	2	TKKMGLLVMAYGTPYKES--DIEPYYTDIRHGKR	42	LKDRYEFI-G----GLSPLA	120	SVGSYDK---RADE
Geobacillus stearothermophilus	2	KNIVGLLVMAYGTPYKED--DIERYYTHIRHGRK	42	LKARYRAI-G----GLSPLA	120	SIRSYNE---RAKA
Exiguobacterium sibiricum	1	MKTLGLLVMAYGTPYKPE--DIERYYTHIRRGRK	41	LTERYEAI-G----GVSPLA	120	SIRSYNG---RAKE
Numidum massiliense	3	TETIGLLVMAYGTPRRPE--DIEPYYTHIRRGKR	43	LKNRYEAI-G----GISPLA	121	SVKSYNG---RAHD
Cohnella thermotolerans	5	NRPIGVLVMSYGTPESLE--GVEAYYTHIRRGHP	45	LTNRYRAIVG----GVFPLR	124	SVGGYLK---RAKE
Corynebacterium diphteriae	18	SDVDAILVLSFGGPEGQQ--DVIPFLENVTRGRG	58	VAVHYRHF-G----GISPLN	134	GCRQYDEDIVRMNH
Mycobacterium tuberculosis	1	MQFDAVLLLSFGGPEGPE--QVRPFLENVTRGRG	41	VAEHYLHF-G----GVSPIN	112	SCTQYVEDIARARR
Rhodococcus jostii	15	SRFDALLVLSFGGPEQPA--DVRPFLENVTRGRG	55	VAEHYLHF-G----GVSPIN	131	GCRQYHEDVARARA
Thermobifida fusca	2	RSYDAFLLISFGGPEKRE--DVIPFLENVTRGRG	42	VGEHYYLF-D----GVSPIN	118	SHRQYLEDIERARA
Leifsonia xyli	27	VAYDAILLAGFGGPEGQD--DVIPFLRNVTRGRG	67	VAQHYRHF-G----GVSPIN	143	SCRQYREDFARVLQ
Micromonospora nigra	1	MAYDAVVLVSFGGPERPE--DVMPFLQNVTRGRG	41	VAEHYLHF-G----GVSPIN	117	SCRQYQEDIAAARA
Lentzea albida	1	MSFDALLWLSFGGPEGPE--DVRPFLENVVRGRG	41	VEAHYQHF-G----GVSPIN	113	ACRQYDEDIVRALQ
Escherichia coli	3	QTKTGILLANLGTPDAPTPEAVKRYLKQFLSDRR	61	VAKLYASV-WME--GGSPLM	135	TVGAVWDELARILA
Klebsiella pneumoniae	3	QTKTGILLANLGTPDAPTPGAVKRYLRQFLSDKR	61	VAKLYQSV-WME--EGSPLM	135	TVAAVWDELARILA
Salmonella enterica	3	QTKTGILLANLGTPDAPTPEAVKRYLRQFLSDQR	61	VAKLYQSI-WME--DGSPLM	135	TVAAVWDELARILA
Bradyrhizobium japonicum	18	QKRVGVLLVNLGTPDTADAPGVRVYLKEFLSDAR	76	KALDYQKI-WNNEKNESPLK	155	TSATVCDEVFRVLA
Nitrobacter winogradskyi	18	RERVGVLLVNLGTPDTADARGVRVYLKEFLSDPR	76	KALDYLKI-WNTELDESPLK	155	TSATVCDEAFRILS
Burkholderia plantarii	14	AHRVAVLLVNLGTPDEPTPGAVRRYLAQFLSDPR	72	SAKKYRSV-WMP--EGSPLR	150	TTATAFDAAFAALG
Methyloferula stellata	24	GGRIGVLLVNLGSPSGTDYWSMRRYLKEFLSDRR	82	KGTDYAAI-WNKARDEAPLK	167	TSATVCDKAFEVLS
Anabaena cylindrica	1	MGRVGVLLLNLGGPDKLE--DVGPFLYNLFSDPE	57	SQENYKYI-G----GGSPLR	133	TSGSSFRLLEQLWR
Cyanothece sp. PCC 7425	1	MGRIGVLLLNLGGPDQLE--DVRPFLYNLFSDPE	57	SQQNYRLI-G----GGSPLR	133	TSGSSFRLLEDLWQ
Gloeobacter violaceus	1	MAEVGVLLLNLGGPDKQE--DVRPFLYNLFADPE	57	SRKNYQAI-G----GGSPLR	133	TSGSSFKLLDQIWA
Leptolyngbya boryana	1	MGRVGVLLLNLGGPDKIE--DVRPFLYNLFADPE	57	SQENYMQI-G----GGSPLR	133	TSGSSFRLLEQLWE
Synechococcus sp. PCC 6312	1	MGRTGVLLLNLGGPDSLA--DVRPFLYNLFSDPE	57	SEANYAQI-G----GGSPLR	133	TSGSSFRLIESLWQ
Chamaesiphon minutus	1	MGRLGVLLLNLGGPEQLS--DVRPFLFNLFSDPE	57	SQANYEKI-G----GGSPLR	133	TSGSSFRLIEKIWS
Calothrix sp. PCC 7103	1	MVRVGVLLLNLGGPDKLD--DVGPFLYNLFSDPE	57	SQENYKQI-G----GGSPLR	134	TSGSSFRLLEQMWK

Fig. 2. (A) Structure of *Lm*CpfC in complex with coproheme (pdb-code: 6SV3). The overall structure is shown on the right and a zoom of the substrate and product binding site on the left. Coproheme is depicted as grey sticks, amino acid residues involved in propionate interactions are shown as green sticks and the secondary structure is represented as cyan cartoon. The figure was prepared using PYMOL (http://www.pymol.org). (B) Adapted sequence alignment of monoderm CpfCs and diderm PpfCs [5]. The relevant residues for propionate interactions in *Lm*CpfC are highlighted in dark blue, if conserved, and in light blue if not. The numbering on top refers to the *Lm*CpfC sequence.

numbering) are also conserved throughout all monoderm and diderm representatives (Fig. 2B, sequence alignment).

We hypothesised that the hydrogen-bonding networks connecting several polar amino acid side chains with the propionate groups are decisive for substrate binding and specificity as well as product delivery. The propionates at positions 2 (p2) and 4 (p4), which are missing in protoporphyrin IX, exhibit numerous H-bonding interactions. p4 interacts with three potential H-bonding partners (T14, Y46, S53) and p2 with Y124, while the propionates at positions 6 and 7, which are also present in protoporphyrin IX, interact with R45 and R29, respectively. Previous studies, investigating point mutations of firmicute CpfCs (from *B. subtilis* and *S. aureus*), were targeting the iron binding and regulatory sites, which are found on the distal side and consist of a histidine and a glutamate residue [11,17,22]. For example, in *B. subtilis* the S54A variant (S53 in *Lm*CpfC) showed a reduced growth rate and coproporphyrin III accumulation in the medium [15]. Interestingly, the loop harbouring S53 in *Lm*CpfC is present in different orientations, when comparing the apo- (pdb-code: 6RWV) with the coproheme-bound *Lm*CpfC (pdb-code: 6SV3) structures [5].

We designed seven mutants of the CpfC from *L. monocytogenes* (*Lm*CpfC), in which H-bonding interactions to the propionate groups in positions 2, 4, 6 and 7 were selectively eliminated. In detail, we have built the Y124F variant (p2), the T14V, Y46F, S53A single and the T14V/Y46F/S53A (TYS) triple variants (p4), the R45L (p6) and the R29L variants (p7) to evaluate the contribution of these residues to the substrate binding and the impact on the stability of the CpfC complexes with coproheme and coproporphyrin III with respect to the wild-type (WT). Additionally, we compared the CpfC complexes and complex formations of protoporphyrin IX, coproporphyrin III, haeme *b* and coproheme to the WT *Lm*CpfC. We have studied this set of WT and variant *Lm*CpfCs comprehensively, by employing circular dichroism, UV–vis electronic absorption and resonance Raman (RR) spectroscopies, differential scanning calorimetry (DSC), pre-steady state kinetic investigations of substrate and product binding, and activity assays of ferrous iron insertion. We further followed the product (coproheme) transfer from *Lm*CpfC WT and variants to *Lm*ChdC, for which coproheme is the substrate. Altogether, this work highlights the importance of non-covalent interactions for substrate and product binding and ultimately elucidates the driving forces, which dictate the substrate specificity for firmicute CpfCs towards four propionate porphyrins.

Results

Spectroscopic signatures and stability of WT *Lm*CpfC complexes

Monodisperse *Lm*CpfC WT was obtained in high yield after expression in *Escherichia coli* and affinity chromatography purification (~ 150 mg L^{-1} of *E. coli* culture) [5]. With the knowledge of the CPD haeme biosynthesis pathway [3], and the experimental studies performed prior to 2015, in which monoderm CpfCs were investigated using protoporphyrin IX (ppIX) as substrate, we reconstituted *Lm*CpfC with coproporphyrin III (cpIII), coproheme, ppIX, and haeme *b* for biochemical investigations (Fig. 3). The UV–vis spectrum, of *Lm*CpfC WT in complex with cpIII (Fig. 3A, red line) exhibits a Soret maximum at 405 nm and Q-bands at 507, 545, 560, and 611 nm. The coproheme-*Lm*CpfC complex (Fig. 3A, brown line) has its Soret maximum at 397 nm with bands in the visible region at 497, 527, and 616 nm. This spectrum is similar to the one obtained with haeme *b* (401, 504, 532, 621 nm; Fig. 3A, black line), which has two vinyl groups instead of the propionate groups at positions 2 and 4 of the porphyrin macrocycle. Due to the vinyl conjugation a red-shift of the bands is expected [23,24]. The same trend is observed in the ppIX bound *Lm*CpfC WT UV–vis spectrum (412, 510, 548, 573, 626 nm; Fig. 3A, blue line).

The differences in the electronic configuration of the *Lm*CpfC's porphyrin binding site becomes even more evident when electronic circular dichroism spectra of all four investigated *Lm*CpfC WT complexes in the near-UV and visible region (260–500 nm) are recorded (Fig. 3B). *Lm*CpfC complexes with four propionate ligands (cpIII and coproheme) show Soret bands with positive ellipticities with maxima at 397 nm (cpIII) and 400 nm (coproheme). The ppIX-*Lm*CpfC WT complex has a significantly red-shifted Soret maximum with a positive ellipticity at 420 nm, whereas the haeme *b* bound protein has a Soret minimum at 393 nm. This significant difference emphasises that the active site architecture is diverse in complexes with haeme *b* and ppIX, which have two vinyl and two propionate groups, compared to the four propionate porphyrins [25,26].

The binding kinetics of the complex formations clearly shows that the presence of propionates at positions 2 and 4 of the tetrapyrrole ring is beneficial for fast and efficient binding (Fig. 3C). The k_{on}-rate for cpIII binding to *Lm*CpfC WT ($68.5 \pm 1.6\ \mu\mathrm{M}^{-1}\cdot\mathrm{s}^{-1}$) is the highest for all four tested ligands, followed by coproheme ($56.6 \pm 0.1\ \mu\mathrm{M}^{-1}\cdot\mathrm{s}^{-1}$). Binding of ppIX

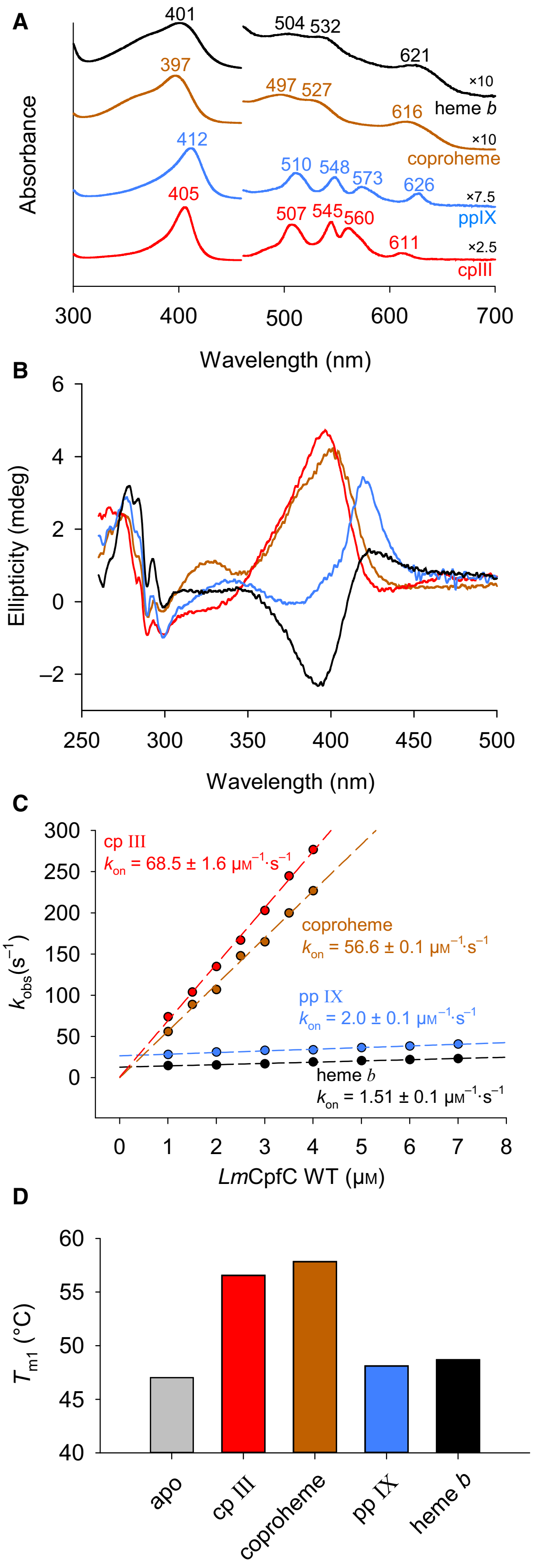

Fig. 3. *Lm*CpfC WT in complex with copropoprhyin III (cpIII; red), iron coproporphyrin III (coproheme; maroon), protoporphyrin IX (ppIX; blue) and iron protoporphyrin IX (haeme *b*; black). (A) UV–vis spectroscopic and (B) electronic circular dichroism spectroscopic signatures of all *Lm*CpfC complexes in the visible region. (C) Plots of k_{obs} *versus* *Lm*CpfC WT concentrations for the determination of binding constants of all four tested ligands. (D) Thermostability of all four *Lm*CpfC WT complexes and the apo-protein (grey), determined by DSC.

and haeme *b* to *Lm*CpfC is significantly slower (35-fold and 45-fold, respectively) with k_{on}-rates of $2.0 \pm 0.1\ \mu\text{M}^{-1}\cdot\text{s}^{-1}$ (ppIX) and $1.5 \pm 0.1\ \mu\text{M}^{-1}\cdot\text{s}^{-1}$ (haeme *b*).

The propionates at positions 2 and 4 of cpIII and coproheme interact with *Lm*CpfC amino acid residues, which results in a higher stability compared to that of the apo-protein [5]. Here, we also tested the thermostability of *Lm*CpfC WT complexes with ppIX and haeme *b* by DSC. In contrast to cpIII and coproheme complexes, which are stabilised by 9.6 °C and 10.8 °C, respectively, ppIX and haeme *b* complexes only show a very modest increase in T_m-values of 1.1 °C and 1.7 °C, respectively, compared to the apo-protein (Fig. 3D).

Furthermore, we investigated the coproheme complexes of the WT and the variants by UV–vis and RR spectroscopies to identify the vibrational signatures of the four propionates via their $\delta(C_\beta C_c C_d)$ bending modes and the effect on the stability upon disruption of the H-bonds by checking the coordination and spin states of the Fe atom (Figs 4 and 5A–D).

The UV–vis spectrophotometric titration in solution at room temperature of the native form (WT) and the variants of *Lm*CpfC with coproheme gave similar final spectra, corresponding to the fully bound substrate-protein complexes. These spectra were obtained with a coproheme : apo-protein ratio ranging from 1 : 1.1 to 1 : 1.6, except for Y124F (ratio 1 : 3). The final spectra of the WT, as described above (Fig. 3A), and the variants (Fig. 6) are typical of high spin (HS) species.

The corresponding RR spectra in the high frequency region at room temperature (Fig. 4, top) are also very similar, except for the Y124F mutant. They are clearly showing that the coproheme is fully bound to the respective apo-proteins, as there are no bands due to the free substrate, which is characterised by a sharp Soret band at 390 nm [27]. The spectra are all characterised by core size marker bands typical of a pentacoordinated high spin species (5cHS), with intense core size-marker bands observed at 1372–1375 (ν_4), 1492 (ν_3), 1584–1586 (ν2), and 1630–1631 (ν_{10}) cm^{-1}. The

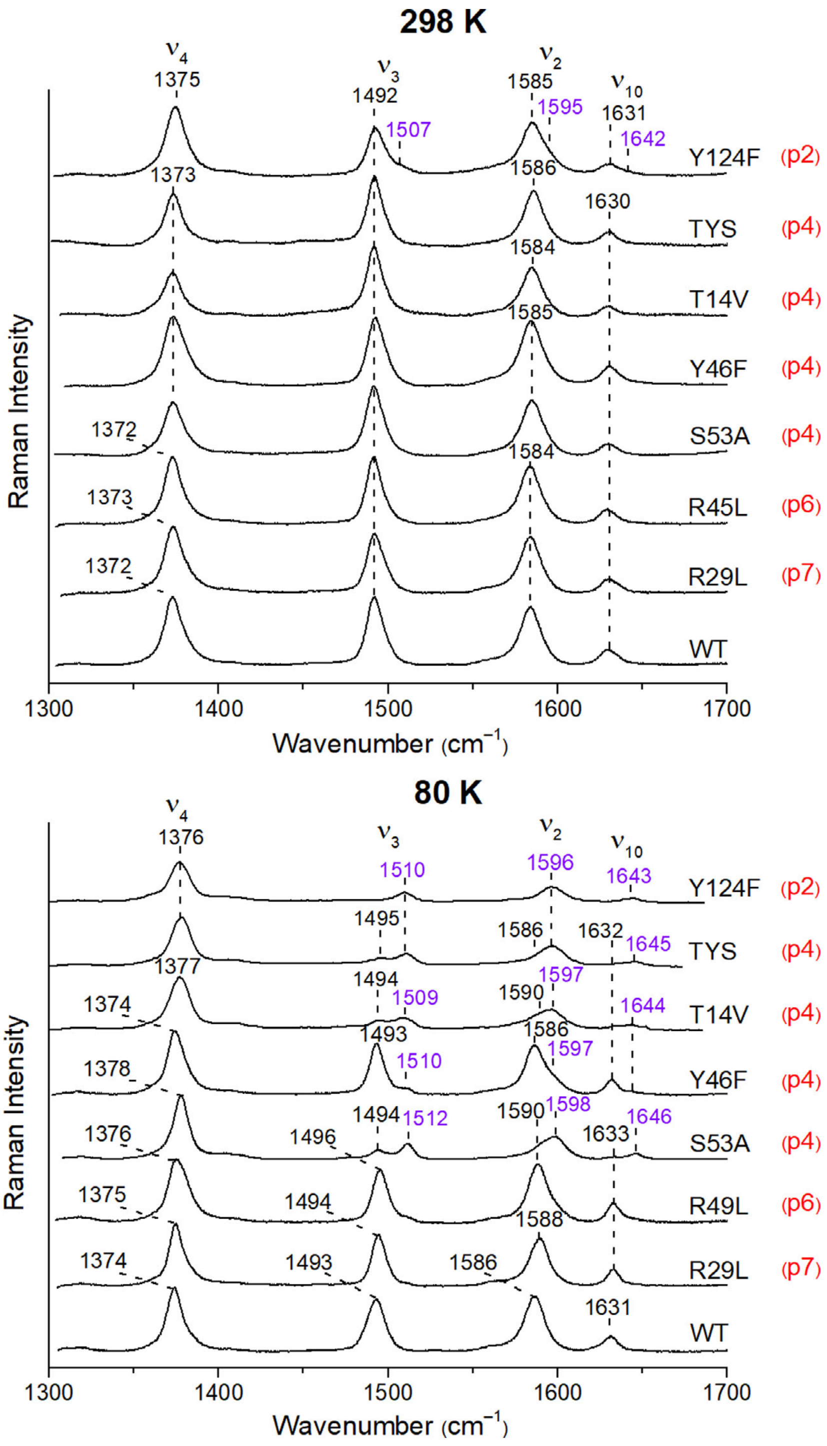

Fig. 4. High frequency RR spectra of coproheme-*Lm*CpfC variants and WT at 298 K (top panel) and 80 K (bottom panel). The RR core-size marker band wavenumbers are reported in black for the 5cHs species and in purple for the 6cLS species, respectively. In red, the is reported the propionate whose H-bond is broken by mutation.

Y124F variant shows the presence of a minor six coordinated low spin (6cLS) species in addition to the 5cHS form. The similar intensity of the ν3 and ν4 bands indicates that in the *Lm*CpfC the iron atom is not linked to a nitrogen atom of an imidazole group [28–30]. These data agree with the structure of the coproheme–*Lm*CpfC complex, which showed that the Fe(III) atom is bound to the oxygen atom of the OH group of the proximal Tyr12 residue [5].

In the 250–450 cm^{-1} frequency region, the RR spectra of the coproheme complexes are characterised by the $\delta(C_{\beta}C_{c}C_{d})$ bending modes of the propionate

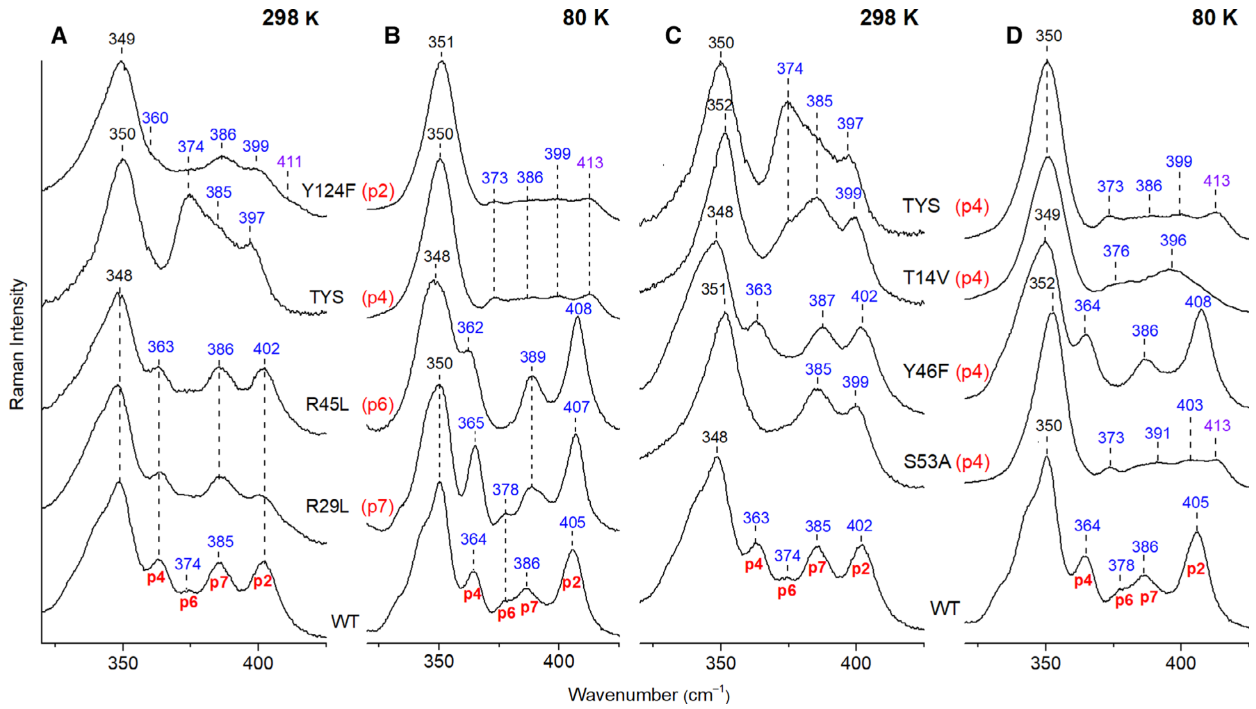

Fig. 5. RR spectra of coproheme-*Lm*CpfC variants and WT (A, B Panels) Low frequency RR spectra of the coproheme complexes of the WT and selected variants on p2, p4, p6 and p7 at 298 K (A) and 80 K (B). (C, D panels) Low frequency RR spectra of the coproheme complexes of the WT and the selected variants on p4 at 298 K (C) and at 80 K (D). The RR porphyrin band wavenumbers are reported in black for the 5cHs species and in green for the 6cLS species respectively, while the propionate bending modes $\delta(C_\beta C_c C_d)$ are indicated in blue. The assignment to each propionate is indicated in red.

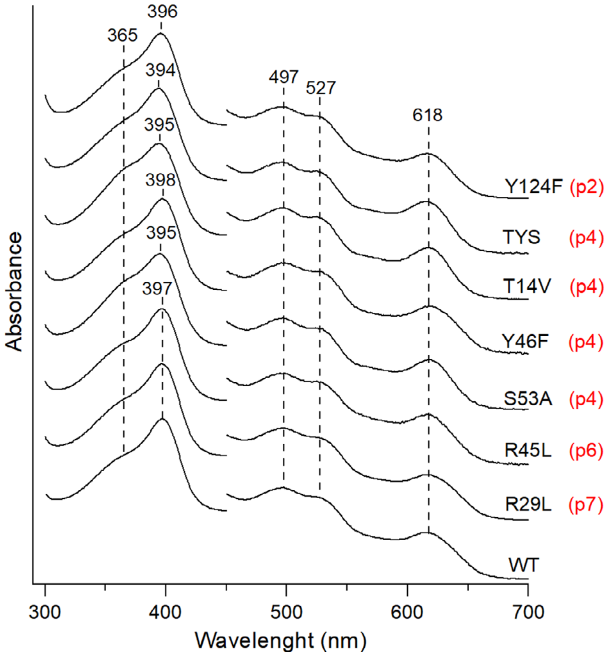

Fig. 6. UV–vis electronic absorption spectra of coproheme-*Lm*CpfC variants and WT at room temperature. In red is reported the propionate whose H-bond is broken by mutation.

groups. As shown in Fig. 5A,C, in the WT complex these modes give rise to three well-defined and intense bands at 363, 385, and 402 cm^{-1}, and a very weak band at 374 cm^{-1}. This confirms that the four propionate groups of coproheme in the *Lm*CpfC WT form hydrogen bonds with different strength with the amino acids of the cavity, in accordance with the structure of the coproheme-*Lm*CpfC complex [5]. In fact, the frequencies of the bending modes of the propionate groups are related to the strength and number of hydrogen bonds between the propionate and the amino acids: the stronger the hydrogen bond is, the higher the frequency [31–33]. Thus, by selectively eliminating the H-bonds by mutation, frequency changes of the propionate bending modes are expected.

The single T14V, S53A and the T14V/Y46F/S53A (TYS) triple variants involved in H-bonds with p4 clearly show the disappearance of the 363 cm^{-1} band, which shifts towards lower wavenumbers, as also indicated by the upshift by 2–4 cm^{-1} of the ν_8 band (at 348 cm^{-1} in the WT) and its broadening. Therefore, this band is assigned to the bending mode of p4. On the contrary, the Y46F mutant RR spectrum is similar to that of the native form (Fig. 5C).

The Y124F mutant shows a strong intensity decrease of the band observed at 402 cm^{-1} in the WT, which shifts to 399 cm^{-1} (Fig. 5A). This band is, therefore, assigned to the bending mode of p2. In addition, the band at 363 cm^{-1}, assigned to p4 downshifts to 360 cm^{-1} and is less intense than in the WT. Interestingly, a similar behaviour (i.e., a decrease in intensity together with a downshift in wavenumbers of the band assigned to p2) is also observed in the variants involved in H-bonds with p4, strongly suggesting a coupling between the p2 and p4 H-bonds.

On the other hand, the low frequency RR spectra of R29L and R45L variants are identical to that of the WT coproheme complex and, therefore, do not allow us to assign the bending modes of the p6 and p7 groups (Fig. 5A). As it was not possible to assign all the $\delta(C_{\beta}C_{c}C_{d})$ bending modes of the propionate groups at room temperature, to increase the spectral resolution, we performed RR measurements of the coproheme complexes of the WT and all the variants at 80 K, since the band widths decrease as the temperature is lowered [31].

The analysis of the high frequency RR spectrum of *Lm*CpfC-complexes with coproheme at 80 K (Fig. 4) shows that the variants involved in the H-bond with p4 (i.e., the single T14V, Y46F, and S53A and the tripleT14V/Y46F/S53A variants), have an increase of an additional 6cLS population in equilibrium with the 5cHS. Further, the Y124F mutant, where the presence of a minor 6cLS population was already observed at room temperature, at low temperature becomes a pure 6cLS species. It is well-known that haeme proteins may undergo a temperature induced transition from high to low spin [31,34]. However, this effect is solely observed in the variants where H-bonds to p2 and p4 have been eliminated.

In the low frequency region, upon decreasing the temperature (down to 80 K), the four well-defined bands observed at 364, 378, 386, and 405 cm^{-1} are assigned to the $\delta(C_{\beta}C_{c}C_{d})$ propionate bending modes of the WT complex; their corresponding wavenumbers are altered by the selective mutations (Fig. 5B,D). In detail, (a) the R29L mutant, as already observed at room temperature, is similar to the complex of the native form (Fig. 5B); (b) in the R45L mutant the band observed at 378 cm^{-1} in the WT, shift towards lower wavenumbers and overlaps with the p4 band, giving rise to a strong band at 362 cm^{-1} (Fig. 5B). Therefore, this band is assigned to the bending mode of propionate p6. For the mutants involving the propionates p2 and p4, the appearance of the low spin species entails the presence in the RR spectrum of a very intense band at 413 cm^{-1} (as previously observed [31]), which makes it difficult to evaluate the relative intensities of the bands in this region (Fig. 5B). However, their propionate bending modes have been clearly assigned at room temperature, and the effect of mutation observed at room temperature are still present at low temperature. Finally, the remaining unassigned band observed at 385 cm^{-1} in the WT (at room temperature) is attributed to the bending mode of p7. Table 1 reports the H-bond distances between the propionate and the residue under investigation together with the frequency of the assigned propionate bending modes.

Thermostability of WT apo-*Lm*CpfC, cpIII and coproheme complexes in comparison with all variants

Monomeric *Lm*CpfC exhibits two endothermic transition upon thermal unfolding. The first one was shown to be associated with the unfolding of the cpIII and coproheme binding site, as the addition of either ligand significantly increased this first T_m-value. The second one did not vary significantly [5], this transition

Table 1. RR frequency of the propionate $\delta(C_{\beta}C_{c}C_{d})$ bending modes (in cm^{-1}) at room and low temperature together with the H-bond distances between the residues and the oxygen atom of the propionate, as determined in the crystal structure of the CpfC from the firmicute *Listeria monocytogenes* (*Lm*CpfC) [5].

	p2		p4		p6		p7		
	RT	LT	RT	LT	RT	LT	RT	LT	H-bond distance (Å)
WT	402	405	363	364	374	378	385	386	
Y46F (p4)	402	408	363	364	–	–	387	386	Tyr46-O_2 2.6
S53A (p4)	399	403	–	–	–	373	385	391	Ser53-O_2 2.9
T14V (p4)	399	396	–	–	374	376	385	–	Thr14-O_1 2.4
T14V Y46F S53A (p4)	397	399	–	–	374	373	385	386	
Y124F (p2)	399	399	360	–	374	373	386	386	Tyr124-O_2 3.1
R45L (p6)	402	408	363	362	–	–	386	389	Arg45-O_1 2.9
R29L (p7)	402	407	363	365	–	378	386	389	Arg29-O_1 2.9

is therefore assumed to describe the final unfolding of the remaining secondary structural elements, after the opening of the proposed porphyrin binding site. In this work, we probed the thermostability of all variants. The apo-form of the *Lm*CpfC variant Y124F, in which the H-bond to p2 is eliminated, exhibits only a marginally decreased melting point of the first transition compared to apo-*Lm*CpfC WT. Most strikingly, upon binding of cpIII or coproheme the thermograms of *Lm*CpfC Y124F are not altered, in contrast to all other *Lm*CpfC samples (Fig. 7A).

The effects observed for the other variants are not as significant as for the Y124F. The interactions to p4 were altered by creating four different variants; T14V, Y46F, S53A, and a triple variant (TYS), which combines all three mutations. The Y46F appears almost WT-like, only the stabilisation upon binding of cpIII or coproheme is not as large as for the WT protein. The other three variants are stabilised by the addition of iron containing coproheme, whereas no such effect can be seen upon binding of cpIII in T14V and the triple variant (TYS) and only a minor stabilisation is observed in the S53A variant (Fig. 7B).

The R45L variant is targeting the interaction to p6. For this variant all determined T_m-values are at lower temperatures, compared to the WT, but the pattern of stabilisation upon binding cpIII or coproheme is the same. In the variant, which likely alters non-covalent interactions to p7 (R29L), no essential effect on stabilisation, compared to the WT protein is observed (Fig. 7B).

Binding kinetics of cpIII and coproheme to WT *Lm*CpfC and variants

The binding reaction of cpIII and coproheme to *Lm*CpfC WT was already shown in Fig. 3C. An overview of all k_{on}-rates for binding of the substrate cpIII and the product coproheme is given in Fig. 8A. All the pseudo-first order rate kinetics plots for cpIII and coproheme binding are presented in Fig. 8B (cpIII) and Fig. 8C (coproheme). Rate constants for k_{on} vary for cpIII binding from 3.2×10^6 $\text{M}^{-1}\cdot\text{s}^{-1}$ (Y124F) to 6.9×10^7 $\text{M}^{-1}\cdot\text{s}^{-1}$ (WT); for coproheme the k_{on}-values vary from 8.9×10^6 $\text{M}^{-1}\cdot\text{s}^{-1}$ (Y124F) to 5.7×10^7 $\text{M}^{-1}\cdot\text{s}^{-1}$. The Y124F mutation, which eliminates the H-bonding interaction to p2, has the largest impact on porphyrin binding, followed by the R45L variant, which targets p6 and eliminates a positive charge on the protein surface, and R29L (p7). The variants targeting p4 bind the respective porphyrins slower than the WT, but appear to be the least affected with k_{on}-rates ranging from 3.5×10^7 $\text{M}^{-1}\cdot\text{s}^{-1}$ to 5.5×10^7 $\text{M}^{-1}\cdot\text{s}^{-1}$.

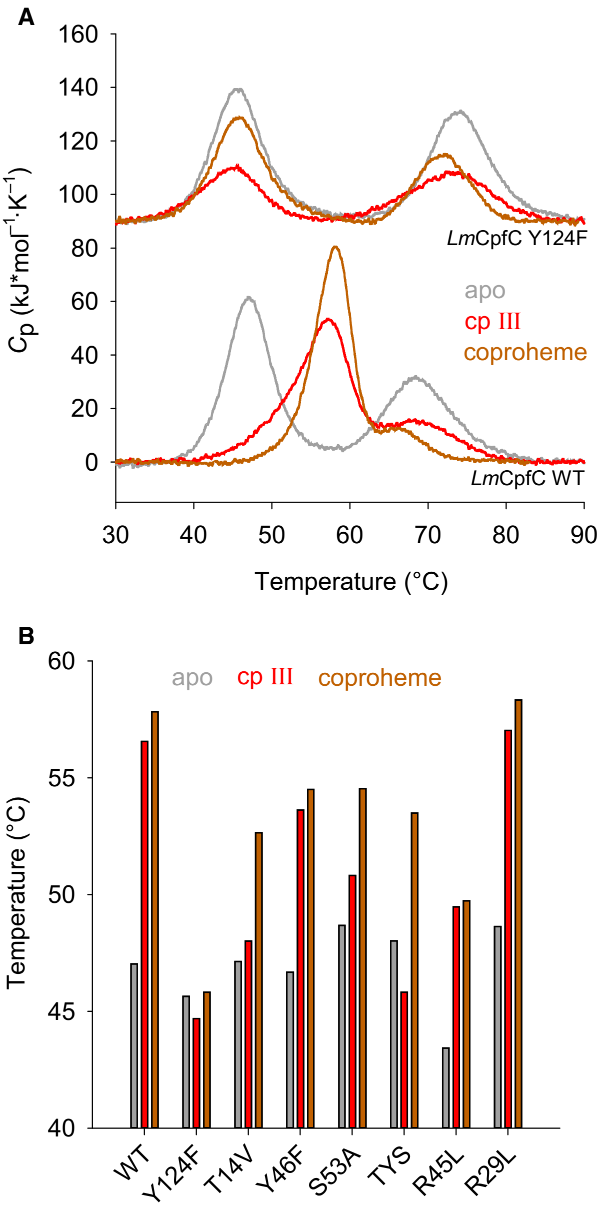

Fig. 7. Thermostability of *Lm*CpfC variants and WT. (A) Representative thermograms showing the endotherms of *Lm*CpfC WT and the Y124F variant of the apo- (grey), cpIII- (red), and coproheme- (maroon) complexes. Thermograms for Y124F were shifted by 90 kJ·mol^{-1}·K^{-1} for better visibility. (B) Overview of the midpoint transitions (T_m-values) of *Lm*CpfC WT and all variants.

The k_{off}-rates (s^{-1}) can be derived from the intercept of the respective plots (Fig. 8B,C). For both substrates, k_{off} for the WT protein is almost zero, indicating a very high affinity, with an estimated K_D-value (K_D = k_{off}/k_{on}) of 1.8 nM for coproheme and 13.0 nM for cpIII. Due to the very low k_{off}, these values have to be considered to only be approximations, as a small deviation of the k_{off}-values would result in a large

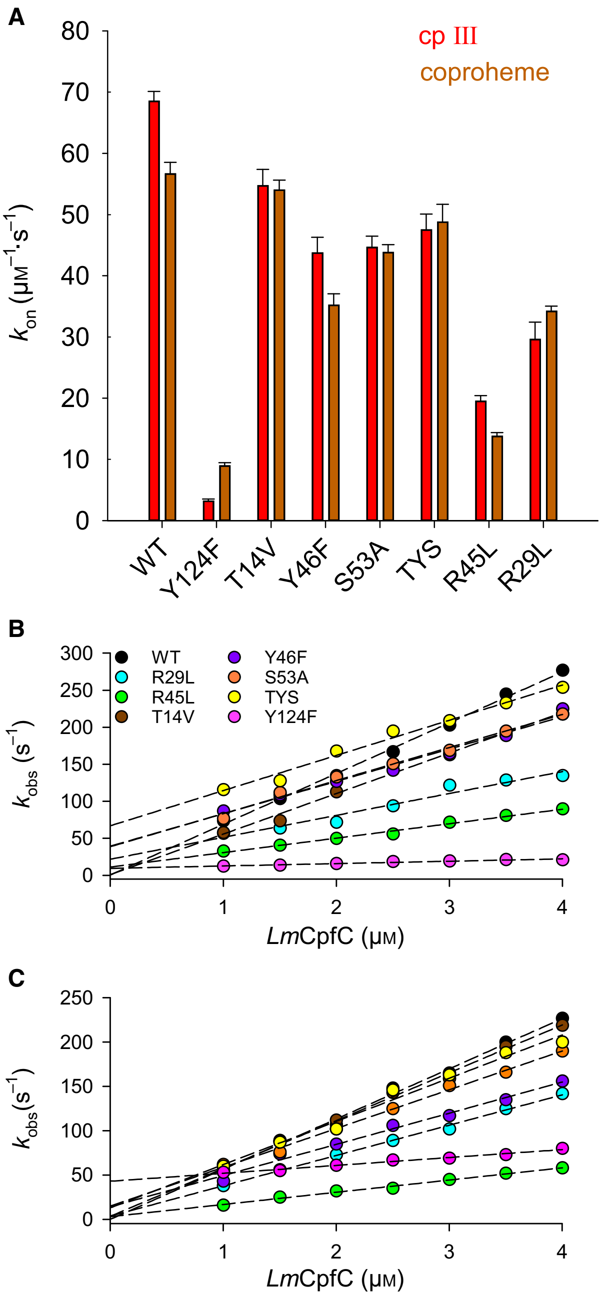

Fig. 8. (A) Overview of binding kinetics of *Lm*CpfC WT and variants. k_{on}-values are presented for all investigated samples and show the bimolecular on-rates (µM^{-1}·s^{-1}) for cpIII (red) and coproheme (maroon) to the respective *Lm*CpfC variant. Error bars are showing standard deviation (SD) of triplicates (*n* = 3) measurements. Binding of coproporphyrin III (B) and coproheme (C) to *Lm*CpfC WT and variants. k_{obs} (s^{-1}) values are plotted against the protein concentrations to derive k_{on} and k_{off} values from the slope (µM^{-1}·s^{-1}) and the intercept (s^{-1}) (C).

change of the K_D-value. A general statement from these binding experiments, concerning the k_{off}-rate, is that all the non-WT *Lm*CpfC variants prove to have a significantly higher k_{off} (ranging from 1.5 to 67.4 s^{-1}) and consequently a lower affinity. This weaker binding is also reflected in the k_{on}-rate, which is the highest for both tested porphyrin ligands for the WT protein.

Transfer of coproheme from WT *Lm*CpfC and variants to WT *Lm*ChdC

After iron insertion by *Lm*CpfC into cpIII, the product, coproheme, needs to be transferred to the enzyme coproheme decarboxylase (*Lm*ChdC) for the last enzymatic step in the CPD haeme biosynthesis pathway. This process can be mimicked *in vitro* by titrating *Lm*ChdC WT to coproheme-loaded *Lm*CpfC WT and variants. These experiments were performed in order to identify the importance of the investigated variants for retaining the product in *Lm*CpfC. Figure 9 shows representative data from WT *Lm*CpfC of this competition binding assay, in which the concentration of *Lm*ChdC WT is constantly increased. The initial UV–vis absorption spectrum (Fig. 9A) clearly resembles the coproheme-bound *Lm*CpfC spectrum (black line), whereas the last spectrum (red line) is identical to that of the *Lm*ChdC coproheme complex. The inset of Fig. 9A shows the plot of the absorbance at a fixed wavelength (375 nm) in the Soret region *versus* the *Lm*ChdC concentration. Hyperbolic fitting of this data allows the calculation of a K_D-value for this extraction and binding process. This approach is a reasonable empirical approximation, which allows to describe the impact of the variants to product transfer to *Lm*ChdC, but is not suited to characterise the ternary complex during the trafficking process. In Fig. 9B, an overview of all K_D-values is given. The extraction of coproheme to *Lm*ChdC is the easiest in the *Lm*CpfC Y124F variant (targeting p2), followed by variants targeting p4 and p6. Interestingly, elimination of a positive charge on the protein surface (*Lm*CpfC R29L), makes it more difficult for *Lm*ChdC to extract coproheme out of this *Lm*CpfC variant, in which the H-bonding to p7 is altered. Data of analogous experiments of *Lm*CpfC WT and all other variants, including hyperbolic fits, is presented in Fig. 9C.

Iron insertion ability of *Lm*CpfC WT and variants

The enzymatic functionality of *Lm*CpfC WT and variants was tested under anaerobic conditions by titration of ferrous iron (0.2–10.0 µM) to 4 µM cpIII in presence of 0.4 µM *Lm*CpfC WT or the respective variants. In Fig. 10A, the spectral transitions from mainly free cpIII (black line) to free coproheme (red line) are shown, while the inset depicts the change in

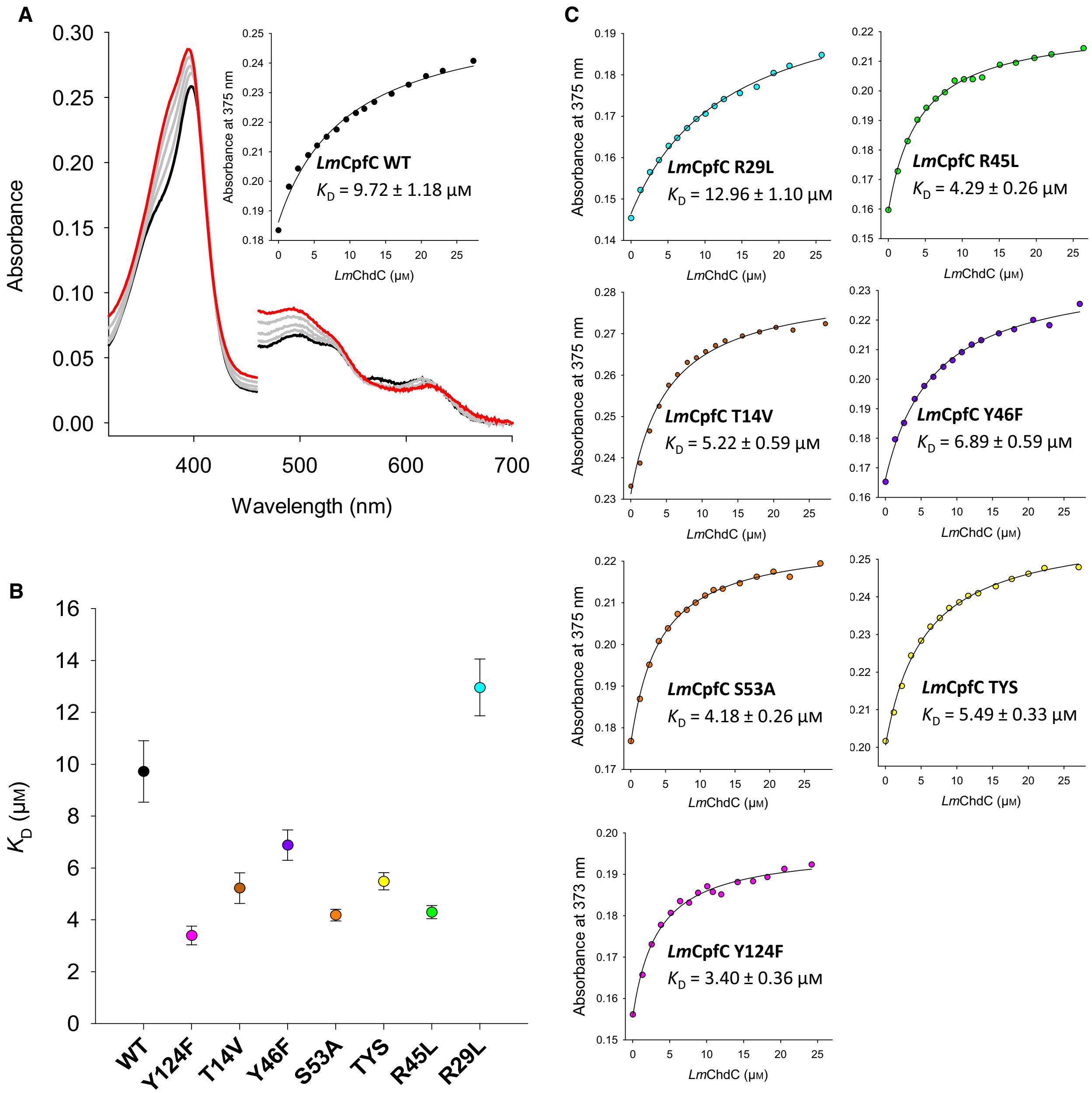

Fig. 9. Coproheme transfer from *Lm*CpfC WT and variants to *Lm*ChdC. (A) Representative titration is monitored using UV–vis absorption spectroscopy of *Lm*CpfC S53A variant, reconstituted initially with coproheme (black spectrum), with *Lm*ChdC WT. The final spectrum is reported in red and shows the coproheme bound to *Lm*ChdC. Spectra in between are represented as grey lines. The inset depicts the change in absorbance at 375 nm with increasing concentrations of *Lm*ChdC. (B) Overview of determined K_D-values of coproheme towards *Lm*ChdC when extracted from *Lm*CpfC WT or variants. Error bars are showing standard deviation (SD) of triplicates (*n* = 3) measurements. (C) Change in absorbance at 375 nm with increasing concentrations of LmChdC for all LmCpfC variants.

absorbance at 393 nm over the ferrous iron concentration for the reaction catalysed by WT *Lm*CpfC. The titrations of all other samples are represented in Fig. 10B. In summary, all the investigated *Lm*CpfC variants show catalytic activity and are able to insert ferrous iron into cpIII. The triple variant (TYS) targeting p4 reaches coproheme saturation at higher ferrous iron concentrations than the other samples.

Discussion

In the CPD dependent prokaryotic haeme biosynthesis pathway, cpIII is the substrate for the CpfC. Prior to

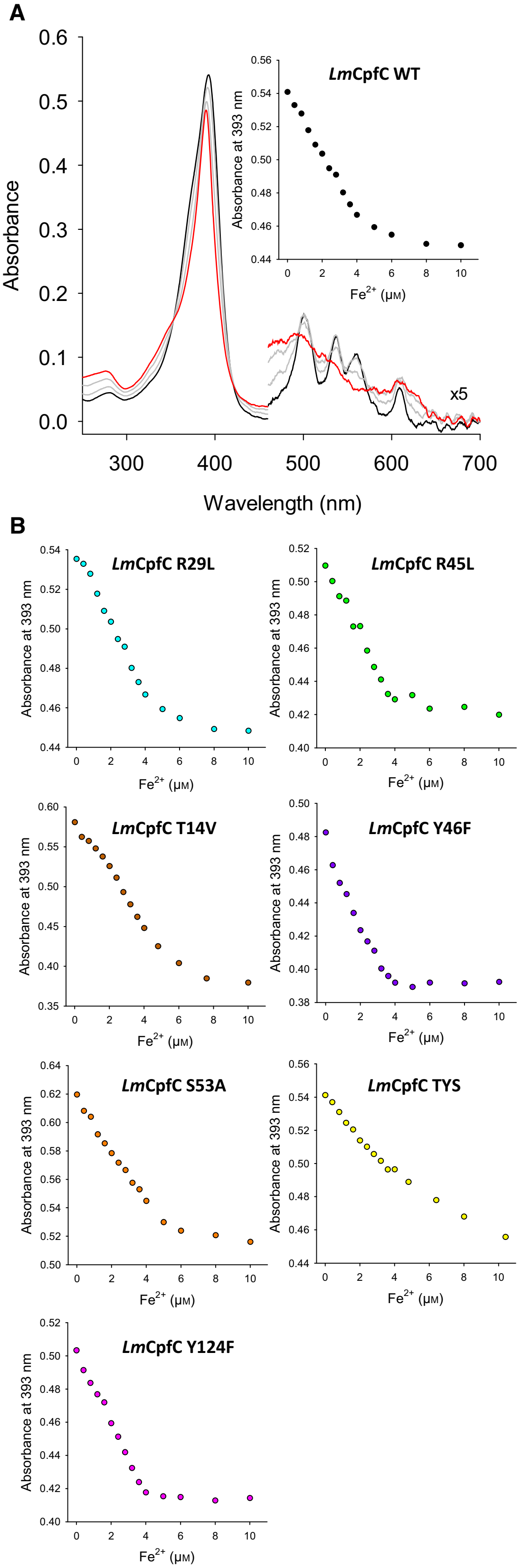

Fig. 10. (A) Activity of *Lm*CpfC WT. The titration under anaerobic conditions of *Lm*CpfC WT, reconstituted with cpIII, was followed by UV–vis absorption spectroscopy. The starting spectrum (black line) shows the cpIII-*Lm*CpfC WT complex, which transforms upon addition of ferrous iron to the coproheme-*Lm*CpfC WT complex (red line). Spectra during the transition are depicted as grey lines. The inset shows the change in absorbance at 390 nm as increasing the concentration of ferrous iron. (B) Change in absorbance of all *Lm*CpfC variants at 390 nm with increasing concentration of ferrous iron. (C) Change in absorbance at 375 nm with increasing concentrations of LmChdC for all LmCpfC variants.

the discovery of the CPD pathway in 2015 [3,7], ferrochelatases of monoderm bacteria were believed to utilise ppIX as substrate. Already in 1994, Hansson and co-workers observed that the porphyrin oxidase (formerly known as HemY) from the monoderm bacterium *B. subtilis*, can oxidize coproporphyrinogen III at a 12-fold higher rate than protoporphyrinogen IX to yield cpIII and ppIX, respectively [34]. In retrospective, this was the very first indication of a second important haeme biosynthesis pathway in prokaryotes. The breakthrough discovery that ChdC acts as the ultimate enzyme in the CPD pathway, implies that the ferrochelatase needs to insert ferrous iron beforehand into a four propionate tetrapyrrole [7,19]. Here, we demonstrate by spectroscopic, thermodynamic, and kinetic methods that *Lm*CpfC clearly favours the four-propionate substrate (cpIII) and four-propionate product (coproheme) over ppIX and haeme *b*. This becomes evident by the significantly faster binding rates to the protein, by the highly increased thermostability of the cpIII- and coproheme-*Lm*CpfC complexes compared to the apo-, ppIX-, and haeme *b*-*Lm*CpfC, and by the distinct spectroscopic signatures (Fig. 3). These data strengthen the fact that cpIII is the physiological substrate of monoderm ferrochelatases.

Therefore, the designed variants of *Lm*CpfC, based on the published crystal structure [5], targeting all the potential residues coordinating the propionates, aim at modifying the substrate and product coordination and specificity. All the selected residues were exchanged to amino acids of similar sizes, but with altered functionality, to maintain the steric constraints as much as possible.

From the structural data, only one tyrosine residue at position 124 was identified to interact with p2. This residue is conserved throughout the monoderm representatives (Fig. 2B) and, as our data show, is the most important for substrate specificity. The spectroscopic signatures of the cpIII and coproheme complexes prove that Y124F is still able to bind the ligands, but with a severely reduced affinity as compared to the WT and the other variants.

The RR spectra of the coproheme complex clearly show that Y124F loses interactions to p2, since its propionate bending mode at 402 cm^{-1} (in WT), shifts to 399 cm^{-1} and decreases in intensity (Fig. 5). Without Y124, the thermostability of the cpIII and coproheme complexes is drastically lowered compared to the WT complexes. There is no stabilisation upon addition of either cpIII or coproheme to the apo-*Lm*CpfC Y124F (Fig. 7). Similarly, there is no stabilisation observed for ppIX and haeme *b* *Lm*CpfC WT complexes compared to the apo-protein (Fig. 3). This demonstrates that the coordination of p2 is crucial for substrate specificity. Further, the cpIII and coproheme binding rates are significantly reduced compared to the WT enzyme (Fig. 8), which emphasises again the importance of this conserved tyrosine residue in monoderm bacteria. The impact of coproheme transfer to *Lm*ChdC is also the biggest of all the investigated variants. Without this tyrosine residue the product coproheme can be extracted very easily to be the substrate for ChdC (Fig. 9). Nevertheless, the Y124F variant can catalyse the insertion of ferrous iron into cpIII (Fig. 10), due to the presence of all catalytic residues on the distal side. This explains why other investigated monoderm ferrochelatases showed activity using ppIX as substrate, prior to the identification of the CPD pathway [11,16].

Structural investigation revealed that in the WT *Lm*CpfC-complex p4 could potentially interact with three amino acids, which are in close proximity (i.e. S53 and Y46 with O2 and T14 with O1) [5]. The spectroscopic signatures of the coproheme complexes of the single variants (T14V and S53A) and the triple variant (TYS), exhibit slight blue-shifts in the Soret bands of the UV–vis absorption spectra, whereas Y46F showed WT-like spectral signatures. Similarly, in the room temperature RR spectra, Y46F displays the same propionate bending vibrations as the WT. The other three variants lack the band in the low frequency region at 363 cm^{-1}, which is, therefore, assigned to the p4 bending mode (Fig. 5C,D). Although we cannot exclude a concomitant compensation in the H-bond strength by the residue T14, which according to the X-ray structure interacts with the same oxygen atom of p4 as the Y46 residue, the spectroscopic data suggest that in solution p4 is coordinated mainly through T14 and S53, rather than Y46.

This hypothesis is strengthened by the thermostability data, where Y46F shows a minor decrease in thermostability, but has no impact on the stabilisation trend in complex with both cpIII and coproheme in contrast to the other variants on p4 [T14V, S53A and the triple variant (TYS)]. In fact, for these latter variants in complex with cpIII, a significant stabilisation compared to the apo-form is hardly observed. This indicates structural differences in the architecture of bound cpIII to *Lm*CpfC in the region of pyrrole ring B, where the propionate substituent (p4) is located. On the other hand, the coproheme complexes of the T14V, S53A and TYS variants display a very similar increase in stability with respect to the apo-form, suggesting that the more rigid product coproheme can be stabilised overall more easily that the flexible cpIII (Fig. 7). Kinetic data on tetrapyrrole binding reveal that disrupting the interactions to p4 does not affect binding to a big extent. All variants showed a similar decrease in binding rates for cpIII and coproheme, least pronounced in T14V. Y46F showed the lowest binding rate of these variants, comparable to S53A (Fig. 8). These findings would lead to the conclusion, that Y46 plays a role in the initial binding of the tetrapyrroles together with S53, but once in complex, T14 takes over and coordinates p4 together with S53, which fits both the spectroscopic and thermostability data. The extraction of coproheme to *Lm*ChdC was affected in the p4 variants and manifested in lower competitive K_D values than for the WT or the R29L variant. Ferrous insertion was not altered in Y46F at all, but T14V and S53 showed a slight impact due to elevated need of ferrous iron for complete turnover. The impact on the triple variant TYS is the biggest. Since Y46F indicated no effect on the insertion process, it is plausible to assume that the combination of the missing T14 and S53 cause the elevated need for ferrous iron (Fig. 10). Although neither T14 nor S53 was shown to be essential for catalysing the insertion of ferrous iron into cpIII, they may play a supportive role in the process.

It is also worth noticing that the RR spectra in the low frequency region show an intensity decrease and a frequency downshift of the bending mode of p4, when the mutation affects the hydrogen bonding network of p2, and *vice versa*, indicating a strong coupling between p2 and p4 (Fig. 5). Furthermore, the variants on p2 and p4 are characterised by a major 6cLS species at low temperature (which in Y124F is partially present already at room temperature) (Fig. 4). The sixth ligand is probably a distal residue of the cavity, further suggesting a major role of these H-bonds in the stabilisation of the protein cavity architecture itself.

The propionate at position 6 (p6) is coordinated by one arginine at the entrance of the binding site, namely R45. The spectroscopic signature in the UV–vis and in the RR spectra at room temperature is found to be similar to the WT. However, since at

80 K in the low frequency region of the RR spectra the band at 378 cm^{-1} (374 cm^{-1} at room temperature) is downshifted, it was assigned to the p6 bending mode (Fig. 5B). The cpIII and coproheme complexes followed the stabilisation trend, but showed a significant decrease in stability, pointing out its significance for complex stabilisation. Surprisingly, the thermostability of the apo variant was the lowest of all generated variants, indicating an additional influence on overall protein thermostability (Fig. 7). The binding rates of the substrate and product decreased by 2.5- and 3.5-fold, respectively. R45 is significant not just for complex stabilisation, but also for a faster and efficient binding of the tetrapyrroles (Fig. 8). In fact, the disruption of the interaction to p6 led to an easier transfer of coproheme to *Lm*ChdC comparable to the variants to p4 (Fig. 9). The ability to insert ferrous iron into cpIII was maintained in the variant (Fig. 10). R45 undergoes a structural rearrangement upon binding of coproheme, as it is evident when comparing the apo- with the coproheme structure [5]. Together with the data presented in this study, we can conclude that the positively charged R45, which is conserved in firmicute CpfCs, is important for the overall stability, the coordination of coproheme via a salt-bridge established to p6, and by attracting the negatively charged substrate during the binding process.

The arginine at position 29 seems to be able to adapt different orientations, when comparing the published crystal structures [5]. In fact, it seems that the coordination effect towards p7 is not always established. That is confirmed by the highly similar cpIII- and coproheme-*Lm*CpfC spectroscopic signatures compared to the WT. Thus, the p7 bending mode in the RR spectra could only be assigned to the band at 385 cm^{-1} (at room temperature), being the only propionate bending mode which remained unassigned both at 298 and 80 K (Fig. 5A,B). The lack of R29 does not affect the thermostability of the variant in its apo and complex-bound forms and exhibits WT-like thermostability characteristics (Fig. 7). The binding rates of cpIII and coproheme are reduced about by 50%, emphasising that the role of the positively charged R29 at the entrance of the binding site is more appropriately described as an attractor for faster and efficient binding of the tetrapyrrole, which has negatively charged propionate groups, or product transfer, rather than as a stabiliser, once bound (Fig. 8). A potential role in product transfer is supported by the elevated need of *Lm*ChdC for complete coproheme delivery (Fig. 9); R29L is the only variant showing such an effect. As anticipated, the catalytic function of the variant was maintained as in all other variants (Fig. 10).

Transfer of the product coproheme from the CpfC to the ChdC was already once tested in another firmicute representative, namely *S. aureus* [21]. The variants of *Sa*ChdC indicated that a surface-exposed tyrosine residue (Y133), a lysine residue (K129) and a glutamate (E120) play a critical role in either protein–protein interaction (ChdC–CpfC) or coproheme retention [21]. Here, we identified a charged residue of CpfC (R45), which is affecting the protein-protein interactions that are presumably critical for coproheme transfer (Fig. 9). It has to be considered that in many monoderm bacteria surface exposed lysines are succinylated or pupylated [35–37]. Succinylation of surface-exposed lysines is a post-translational modification that drastically alters the charge properties (positively charged lysine converts to a negatively charged succinyl) of the protein surface [38]. Not surprisingly, this potentially has a major impact on protein-protein interactions at physiological conditions and has to be studied in detail in the future.

In summary, we present a thorough study that explains the H-bond interactions pattern, which defines the substrate specificity of *Lm*CpfC towards the four propionates of coproporphyrin III and the resulting product coproheme. The study of relevant variants by several biophysical and biochemical methods allowed us to evaluate the contributions of each propionate group. It is demonstrated that a tyrosine residue, interacting with p2 (Y124 in *Lm*CpfC) and conserved in monoderm CpfC representatives, is crucial for cpIII and coproheme binding and coordination. Furthermore, we demonstrate that unlike to what is suggested by the crystal structure [5], in solution p4 is mainly coordinated by T14 and S53. DSC experiments of the T14V and S53A variants imply that the pyrrole ring B of cpIII at the site of p4 is likely to be positioned differently compared to pyrrole ring B of coproheme in complex with *Lm*CpfC (Fig. 7). This might indicate a certain degree of distortion of cpIII, which is supposed to be necessary for efficient insertion of ferrous iron [22,39,40]. The presented data gives a complete overall picture of cpIII and coproheme binding and paves the way for future mechanistic studies on CpfCs.

Materials and methods

Generation, expression and purification of *Lm*CpfC and variants

With the already available plasmid pET21a(+) carrying the *Lm*CpfC sequence and a C-terminal 6 × His-tag [5], site directed mutagenesis was performed with the QuikChange Lightning Kit (Agilent Technologies, Santa Clara, CA,

Table 2. Primers used for site-directed mutagenesis to create *Lm*CpfC variants.

Primer name	Primer sequence
*Lm*CpfC T14V_fw	5′-tgtaatggcatacggagtaccgtataaagatgaagatatcgaacgttac-3′
*Lm*CpfC T14V_rev	5′-gtaacgttcgatatcttcatctttatacggtactccgtatgccattaca-3′
*Lm*CpfC R29L_fw	5′-gaacgttactatacagatattcttcatggtcataagccaagtga-3′
*Lm*CpfC R29L_rev	5′-tcacttggcttatgaccatgaagaatatctgtatagtaacgttc-3′
*Lm*CpfC R45L_fw	5′-attgccgatttacgcggtttataccatgcaatcggcgg-3′
*Lm*CpfC R45L_rev	5′-ccgccgattgcatggtataaaccgcgtaaatcggcaat-3′
*Lm*CpfC Y46F_fw	5′-cgatttacgcggtagattccatgcaatcggcg-3′
*Lm*CpfC Y46F_rev	5′-cgccgattgcatggaatctaccgcgtaaatcg-3′
*Lm*CpfC S53A_fw	5′-catgcaatcggcggactagccccacttgcaaaa-3′
*Lm*CpfC S53A_rev	5′-ttttgcaagtggggctagtccgccgattgcatg-3′
*Lm*CpfC Y46F S53A_fw	5′-cgatttacgcggtagattccatgcaatcggcggactagccccacttgcaa-3′
*Lm*CpfC Y46F S53A_rev	5′-ttgcaagtggggctagtccgccgattgcatggaatctaccgcgtaaatcg-3′
*Lm*CpfC Y124F_fw	5′-tagctttagtgtcgaggctttcaacaaaagagcaaaagaag-3′
*Lm*CpfC Y124F_rev	5′-cttcttttgctcttttgttgaaagcctcgacactaaagcta-3′

USA) according to the manufacturer's protocol to obtain the desired variants T14V, R29L, R45L, Y46F, S53A, the triple variant T14V Y46F S53A (TYS) and Y124F (Primers see Table 2); 2 µL of the DpnI digested reaction was used to transform *E. coli* XL-10 by heat-shock transformation. DpnI digest and heat-shock transformation were performed according to the Agilent Technologies protocol. Plasmids were purified from over-night cultures with the Monarch Plasmid Miniprep Kit (New England Biolabs, Frankfurt/Main, Germany) and the presence of the mutations were verified by SANGER sequencing done by Microsynth AG (Vienna, Austria). Plasmids with correct mutations were re-transformed by heat-shock transformation into the expression strain *E. coli* BL21 Gold.

Expression was done in LB medium supplemented with 1 mM ampicillin and cultivated at 37 °C until an OD_{600} of ~ 0.4–0.6. Then, the cultures were cooled to 24 °C, induced with 0.5 mM IPTG and further to 20 °C for over-night expression.

On the next day, cells were harvested by centrifugation (2430 ***g***) and lysed by sonication (SONOPLUS Bandelin, Berlin, Germany). Cell debris in the lysate were removed by another centrifugation step (38 724 ***g***). The lysate was applied to a HisTrap column and the *Lm*CpfC eluted using an imidazole gradient (0–500 mM). Fractions containing *Lm*CpfC were pooled and buffer exchanged in a 1 × PBS buffer with 100 mM NaCl pH 7.4 using a PD-10 column (GE Healthcare, Vienna, Austria) and stored at −80 °C.

Verification of the monomeric state

Monomeric state of *Lm*CpfC was controlled after each expression by HPLC (Shimadzu prominence LC20, Korneuburg, Austria), equipped with MALS (WYATT Heleos Dawn8 + plus QELS; software ASTRA 6, Dernbach, Germany), refractive index detector (RID-10A; Shimadzu), and a diode array detector (SPD-M20A; Shimadzu). Particle size of the column (Superdex 200 10/300 GL; GE Healthcare) was 13 µm and was equilibrated with 1 × PBS plus 200 mM NaCl and a flow rate of 0.75 mL·min^{-1}. The amount of loaded protein was 80 µg. The correct molar mass calculation performance by MALS was checked by the determination of a sample of bovine serum albumin. This method was applied similarly as previously described [41].

Determination of the extinction coefficient of coproporphyrin III and protoporphyrin IX

Coproporphyrin III dihydrochloride (Frontier Scientific®; Logan, UT, USA; BatchID: JB18-12246) was weighed in three-times independently, dissolved with 0.5 M NaOH and filled up with ddH_2O to a concentration of 1 mM in 1.5 mL reaction tubes. The stocks were diluted to 100 µM, which was used to make three dilution series (0.2–1.1 µM in 0.1 µM steps in 50 mM HEPES pH 7.4). Dilution triplicates were measured using a flame-S-UV-VIS-ES, a DH-2000-BAL UV-VIS-NIR light source and a 1 cm cuvette holder (all Ocean Optics, Ostfildern, Germany). UV–vis absorption spectra were recorded from 700 to 250 nm using the OCEANVIEW software (Ocean Optics). We used the following parameters: integration time 7.5 ms; scans to average 10; electric dark and nonlinearity correction enabled and boxcar width 8. Protoporphyrin IX (Frontier Scientific®; BatchID: JLN15-9933) was weighed in three-times independently, dissolved with 0.5 M NaOH and filled up with ddH_2O to 100 mL in a volumetric flask. The concentration in the stock solution was calculated and used to make three dilution series (2–12 µM in 1 µM steps in 50 mM HEPES pH 7.4) in glass test tubes, because of the sticky behaviour of protoporphyrin IX to plastics. UV–vis spectra (250–700 nm) were recorded using a Cary 60 scanning spectrophotometer (Agilent).

The increase in absorbance at a single wavelength (for coproporphyrin III at 393 nm and for protoporphyrin IX at 373 nm) was plotted over the porphyrin concentration.

A linear regression was applied and the extinction coefficients calculated from the slope of the regression are 150 736 $\text{M}^{-1}\cdot\text{cm}^{-1}$ for coproporphyrin III and 86 168 $\text{M}^{-1}\cdot\text{cm}^{-1}$ for protoporphyrin IX, respectively (Fig. 11). Th extinction coefficients used for free coproheme was 128 800 $\text{M}^{-1}\cdot\text{cm}^{-1}$ at 390 nm [9] and for free haeme *b* was 58 440 $\text{M}^{-1}\cdot\text{cm}^{-1}$ at 385 nm [42].

Reconstitution of *Lm*CpfC complexes

*Lm*CpfC was reconstituted with coproporphyrin III or coproheme by adding a 1.2-fold molar excess of the respective ligand and incubated for 15 min. Samples were transferred into a 0.5 mL Amicon-Ultra Centrifugation Filters (Millipore, Darmstadt, Germany) and filled up with the storage buffer. Samples were centrifuged (15.493 ***g***), the flow through discarded, the filters filled up again with storage buffer and centrifuged again. This procedure was repeated until the lack of free ligand was confirmed by UV–vis spectroscopy of the flow through after the final round. Samples were then stored at −80 °C.

Resonance Raman

The RR spectra were obtained at 298 K using a 5 mm NMR tube by excitation with the 404.8 nm line of a diode laser (MatchBox Series, Integrated Optics, Vilnius, Lithuania). Backscattered light from a slowly rotating NMR tube was collected and focussed into a triple spectrometer (consisting of two SpectraPro 2300i instruments working in the subtractive mode and a SpectraPro 2500i instrument in the final stage with a grating of 3600 grooves/mm by Acton Research Corp., Acton, MA, USA), equipped with a liquid nitrogen-cooled CCD detector.

For the low temperature experiments, a 50 µL droplet of the sample was put in a 1.5 cm diameter quartz crucible inside a THMS600 cryostat (Linkam Scientific Instruments, Surrey, UK) and frozen at 80 K. To avoid either sample denaturation or photo-reduction, the laser position on the sample was changed frequently.

A spectral resolution of 1.2 cm^{-1} and spectral dispersion of 0.40 cm^{-1}/pixel were calculated theoretically on the basis of the optical properties of the spectrometer. The RR spectra were calibrated with indene and carbon tetrachloride as standards to an accuracy of 1 cm^{-1} for intense isolated bands. All the RR measurements were repeated several times under the same conditions to ensure reproducibility. Table 3 summarises the integration time and the number of averaged spectra reported in the figures. All the spectra were baseline-corrected and were normalised to the intensity of the ν_4 band at 1370–1373 cm^{-1} for the high frequency region and to the ν_8 band at 348–352 cm^{-1} in the low frequency region, respectively. The laser power at the sample for the coproheme complex of the WT and all the variants was 7 mW at 298 K, and 5 mW at 80 K, respectively. In the figures, the spectra were shifted along the ordinate axis for the sake of clarity.

Table 3. Integration time and number of averaged RR spectra at 298 and 80 K reported in the figures for the coproheme complex of *Lm*CdfC WT protein and variants.

Protein	Temperature	High frequency (average/integration time)	Low frequency (average/integration time)
WT	298 K	20 spectra/100 min	30 spectra/150 min
	80 K	16 spectra/32 min	35 spectra/70 min
R29L	298 K	12 spectra/60 min	18 spectra/90 min
	80 K	30 spectra/60 min	50 spectra/100 min
R45L	298 K	12 spectra/60 min	20 spectra/100 min
	80 K	20 spectra/40 min	40 spectra/80 min
S53A	298 K	12 spectra/60 min	20 spectra/100 min
	80 K	20 spectra/40 min	20 spectra/40 min
Y46F	298 K	12 spectra/60 min	24 spectra/120 min
	80 K	5 spectra/10 min	40 spectra/80 min
T14V	298 K	10 spectra/50 min	24 spectra/120 min
	80 K	5 spectra/10 min	5 spectra/10 min
TYS	298 K	12 spectra/60 min	30 spectra/150 min
	80 K	16 spectra/32 min	60 spectra/120 min
Y124F	298 K	12 spectra/60 min	19 spectra/95 min
	80 K	4 spectra/20 min	40 spectra/80 min

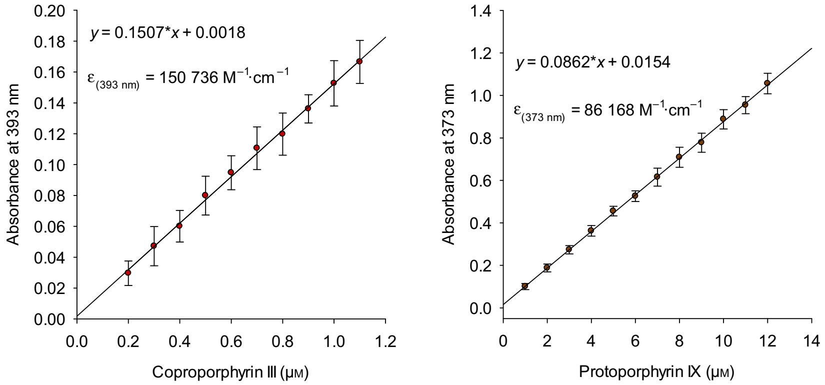

Fig. 11. Determination of the extinction coefficients for cpIII at 393 nm (red circles) and ppIX at 373 nm (maroon circles) in 50 mM HEPES buffer, pH 7.4. Error bars are showing standard deviation (SD) of triplicates (n = 3) measurements.

UV–vis electronic absorption spectra were recorded both before and after RR measurements to ensure that no degradation occurred under the experimental conditions using a 5 mm NMR tube or a 1 mm cuvette (300 nm·min^{-1} scan rate) at 298 K by means of a Cary 60 spectrophotometer (Agilent) with a resolution of 1.5 nm. For calculation of the second derivative spectra, the Savitzky–Golay method was applied using 15 data points (LabCalc, Galactic Industries, Salem, NH, USA). No changes in the wavelength or in the bandwidth were observed, when the number of points was increased or decreased.

Sample preparation for UV-vis and RR experiments

Ferric coproheme was purchased from Frontier Scientific, Inc. (Logan, UT, USA) as lyophilised powder. The samples were prepared by adding the coproheme alkaline solution (coproheme dissolved in 0.5 M NaOH) to apo-*Lm*CpfC dissolved in 50 mM HEPES buffer, pH 7.4. The coproheme : apo-protein ratio was determined by means of UV–vis spectroscopy to ensure the complete binding of the substrate and is reported in the text for all the variants and the WT protein. In all the preparations, a slight excess of apo-protein has been used to avoid the presence of free substrate in solution. In fact, the RR spectrum of the free coproheme is characterised by intense bands, which can overlap with those of the proteins.

The sample concentrations, in the range of 10–40 μM for UV–vis and RR measurements at room temperature, were determined using an extinction coefficient as defined above for the RR experiments at 80 K the concentrations were in the range of 35–210 μM.

Thermal stability of *Lm*CpfC variants and their complexes

Temperature stability experiments were performed by DSC using an automated PEAQ-DSC (Malvern Panalytical, Malvern, UK) equipped with an autosampler for 96-well plates. The cell volume was 130 μL and measurements were controlled by the integrated MIRCOCAL-PEAQ-DSC software (Malvern, UK). The measurements were carried out over a temperature range of 20–100 °C using a programmed heating scan rate of 90 °C·h^{-1} and a cell pressure of ~ 60 psi (4.136 bar). The concentration of samples for the measurements was 14 μM of apo-, coproporphyrin III, or coproheme-*Lm*CpfC in 50 mM phosphate buffer pH 7.4. Thermograms were corrected for sample concentration and buffer baseline. The integrated analysis software was used for data evaluation and conversion. Heat capacity was (C_p) was expressed in kJ·mol^{-1}·K^{-1} and data points were fitted to non-two-state equilibrium-unfolding models by the Lavenberg/Marquardt nonlinear least squares method like it was done similarly as described previously [43].

Kinetics of coproporphyrin III, coproheme, protoporphyrin IX and haeme *b* binding to *Lm*CpfC variants

Ligand binding to apo-*Lm*CpfC was monitored by time-resolved means using a stopped-flow apparatus equipped with a monochromator and a photomultiplier detector (model Pistar-180; Applied Photophysics, Leatherhead, UK) using a 75W Xenon lamp. The volume of the optical quartz cell was 20 μL with 10 mm pathlength. The fastest mixing time was between 1 and 1.5 ms. The concentration of the respective ligand was kept constant in the cell (0.5 μM) and *Lm*CpfC was present in excess (1–4 μM for coproporphyrin III and coproheme; 1–7 μM for protoporphyrin IX and haeme *b*). The experiments were performed in 50 mM HEPES pH 7.4 at 25 °C. Time traces were recorded (in triplicates) at a single wavelength (380 nm for coproporphyrin III; 390 nm for coproheme; 407 nm for protoporphyrin IX and haeme *b*) and fitted double exponentially. The second-order rate constant k_{on} was determined by plotting obtained k_{obs} values *versus* *Lm*CpfC concentration.

Enzymatic activity of *Lm*CpfC variants

Enzymatic activity of the variants was screened spectrophotometrically using a flame-S-UV-VIS-ES, a DH-2000-BAL UV-VIS-NIR light source and a 1 cm cuvette holder (all Ocean Optics) in a Whitley DG250 Anaerobic Workstation (Don Whitley Scientific, Bingley, UK) under anaerobic conditions by titration of ferrous iron [source: iron(II) sulphate heptahydrate; CAS: 7782-63-0; LOT # SLCH2225; Sigma, Vienna, Austria]. UV–vis electronic absorption spectra were recorded from 700 to 250 nm using the OCEANVIEW software (Ocean Optics). We used the following parameters: integration time 7.5 ms; scans to average 10; electric dark and nonlinearity correction enabled and boxcar width 8. The 200 mM ferrous iron stock solutions for the titration were prepared under anaerobic conditions by weighing in a small amount and dissolving it in the calculated volume of degassed ddH$_2$O. From the stock solution a 1 mM ferrous iron solution was prepared, which was used for titration.

The capability of the *Lm*CpfC variants to form coproheme from coproporphyrin III and ferrous iron, as well as the ability to cycle the reaction, was monitored by the spectral shift of free coproporphyrin III (Soret maximum at 393 nm) to free coproheme (Soret maximum at 390 nm). The decrease at 393 nm was plotted against ferrous iron concentration. The titration was performed with 0.4 μM *Lm*CpfC and 4 μM coproporphyrin III (in 50 mM HEPES pH 7.4) by stepwise addition of small ferrous iron aliquots (0–10 μM) in a 1 mL stirrer cuvette until complete turnover. A one minute-waiting time was introduced after each titration step, to ensure the completion of the reaction, before each spectrum was recorded.

Impact of mutations on coproheme transfer

The impact of the different mutations on product transfer from *Lm*CpfC to *Lm*ChdC was probed by a competition binding assay (in 50 mM HEPES pH 7.4). Four micromolar reconstituted *Lm*CpfC with coproheme was titrated with increasing concentrations of *Lm*ChdC (0–25 µM). Two minutes were waited between the titration steps to ensure complete transfer. A Cary 60 scanning spectrophotometer (Agilent) was used to record the UV–vis spectra. Expression and purification of *Lm*ChdC were performed as previously described [27,31]. K_D values were derived by plotting the absorbance of a single wavelength (between 370 and 375 nm mutant dependent) *versus* *Lm*ChdC concentration by fitting to a hyperbolic function.

Acknowledgements

This project was supported by EQ-BOKU VIBT GmbH and the BOKU Core Facility *Biomolecular & Cellular Analysis*. This project was financed by the Austrian Science Fund, FWF, projects P29099, P33544, W1224 (SH) and Fondazione Cassa Risparmio di Firenze, grant 2020.1397 (GS).

Conflict of interest

The authors declare no conflict of interest.

Author contributions

SH and GS planned experiment; TG, FS, JH, and AD performed experiments; TG, FS, SH, AD, PGF, and GS analyzed data; TG, CO, PGF, FS, GS, and SH wrote the paper.

Peer Review

The peer review history for this article is available at https://publons.com/publon/10.1111/febs.16257.

References

1 Ferreira GC, Franco R, Lloyd SG, Moura I, Moura JJ & Huynh BH (1995) Structure and function of ferrochelatase. *J Bioenerg Biomembr* **27**, 221–229.

2 Dailey HA, Dailey TA, Wu CK, Medlock AE, Wang KF, Rose JP & Wang BC (2000) Ferrochelatase at the millennium: structures, mechanisms and [2Fe-2S] clusters. *Cell Mol Life Sci* **57**, 1909–1926.

3 Dailey HA, Dailey TA, Gerdes S, Jahn D, Jahn M, O'Brian MR & Warren MJ (2017) Prokaryotic heme biosynthesis: multiple pathways to a common essential product. *Microbiol Mol Biol Rev* **81**, e00048-16.

4 Pfanzagl V, Holcik L, Maresch D, Gorgone G, Michlits H, Furtmüller PG & Hofbauer S (2018) Coproheme decarboxylases – phylogenetic prediction versus biochemical experiments. *Arch Biochem Biophys* **640**, 27–36.

5 Hofbauer S, Helm J, Obinger C, Djinović-Carugo K & Furtmüller PG (2020) Crystal structures and calorimetry reveal catalytically relevant binding mode of coproporphyrin and coproheme in coproporphyrin ferrochelatase. *FEBS J* **287**, 2779–2796.

6 Layer G (2021) Heme biosynthesis in prokaryotes. *Biochim Biophys Acta Mol Cell Res* **1868**, 118861.

7 Dailey HA, Gerdes S, Dailey TA, Burch JS & Phillips JD (2015) Noncanonical coproporphyrin-dependent bacterial heme biosynthesis pathway that does not use protoporphyrin. *Proc Natl Acad Sci USA* **112**, 2210–2215.

8 Bryant DA, Hunter CN & Warren MJ (2020) Biosynthesis of the modified tetrapyrroles-the pigments of life. *J Biol Chem* **295**, 6888–6925.

9 Hofbauer S, Mlynek G, Milazzo L, Pühringer D, Maresch D, Schaffner I, Furtmüller PG, Smulevich G, Djinović-Carugo K & Obinger C (2016) Hydrogen peroxide-mediated conversion of coproheme to heme b by HemQ-lessons from the first crystal structure and kinetic studies. *FEBS J* **283**, 4386–4401.

10 Celis AI, Streit BR, Moraski GC, Kant R, Lash TD, Lukat-Rodgers GS, Rodgers KR & DuBois JL (2015) Unusual peroxide-dependent, heme-transforming reaction catalyzed by HemQ. *Biochemistry* **54**, 4022–4032.

11 Hansson MD, Karlberg T, Rahardja MA, Al-Karadaghi S & Hansson M (2007) Amino acid residues His183 and Glu264 in *Bacillus subtilis* ferrochelatase direct and facilitate the insertion of metal ion into protoporphyrin IX. *Biochemistry* **46**, 87–94.

12 Dailey HA, Finnegan MG & Johnson MK (1994) Human ferrochelatase is an iron-sulfur protein. *Biochemistry* **33**, 403–407.

13 Medlock AE, Najahi-Missaoui W, Shiferaw MT, Albetel AN, Lanzilotta WN & Dailey HA (2021) Insight into the function of active site residues in the catalytic mechanism of human ferrochelatase. *Biochem J* **478**, 3239–3252.

14 Al-Karadaghi S, Hansson M, Nikonov S, Jönsson B & Hederstedt L (1997) Crystal structure of ferrochelatase: the terminal enzyme in heme biosynthesis. *Structure* **5**, 1501–1510.

15 Olsson U, Billberg A, Sjövall S, Al-Karadaghi S & Hansson M (2002) In vivo and in vitro studies of *Bacillus subtilis* ferrochelatase mutants suggest substrate channeling in the heme biosynthesis pathway. *J Bacteriol* **184**, 4018–4024.

16 Lecerof D, Fodje M, Hansson A, Hansson M & Al-Karadaghi S (2000) Structural and mechanistic basis of

porphyrin metallation by ferrochelatase. *J Mol Biol* **297**, 221–232.

17 Karlberg T, Hansson MD, Yengo RK, Johansson R, Thorvaldsen HO, Ferreira GC, Hansson M & Al-Karadaghi S (2008) Porphyrin binding and distortion and substrate specificity in the ferrochelatase reaction: the role of active site residues. *J Mol Biol* **378**, 1074–1083.

18 Hobbs C, Reid JD & Shepherd M (2017) The coproporphyrin ferrochelatase of *Staphylococcus aureus*: mechanistic insights into a regulatory iron-binding site. *Biochem J* **474**, 3513–3522.

19 Lobo SA, Scott A, Videira MA, Winpenny D, Gardner M, Palmer MJ, Schroeder S, Lawrence AD, Parkinson T, Warren MJ *et al.* (2015) *Staphylococcus aureus* haem biosynthesis: characterisation of the enzymes involved in final steps of the pathway. *Mol Microbiol* **97**, 472–487.

20 Videira MAM, Lobo SAL, Silva LSO, Palmer DJ, Warren MJ, Prieto M, Coutinho A, Sousa FL, Fernandes F & Saraiva LM (2018) *Staphylococcus aureus* haem biosynthesis and acquisition pathways are linked through haem monooxygenase IsdG. *Mol Microbiol* **109**, 385–400.

21 Celis AI, Choby JE, Kentro J, Skaar EP & DuBois JL (2019) Control of metabolite flux during the final steps of heme b biosynthesis in Gram-positive bacteria. *Biochemistry* **58**, 5259–5270.

22 Shipovskov S, Karlberg T, Fodje M, Hansson MD, Ferreira GC, Hansson M, Reimann CT & Al-Karadaghi S (2005) Metallation of the transition-state inhibitor N-methyl mesoporphyrin by ferrochelatase: implications for the catalytic reaction mechanism. *J Mol Biol* **352**, 1081–1090.

23 Marzocchi M & Smulevich G (2003) Relationship between heme vinyl conformation and the protein matrix in peroxidases. *J Raman Spectrosc* **34**, 725–736.

24 Spiro TG & Li X-Y (1988) Resonance Raman spectroscopy of metalloporphyrins. In Biological Applications of Raman Spectroscopy (Spiro TG, ed), pp. 1–37. John Wiley, New York, NY.

25 Kelly SM, Jess TJ & Price NC (2005) How to study proteins by circular dichroism. *Biochim Biophys Acta* **1751**, 119–139.

26 Nagai M, Nagai Y, Aki Y, Imai K, Wada Y, Nagatomo S & Yamamoto Y (2008) Effect of reversed heme orientation on circular dichroism and cooperative oxygen binding of human adult hemoglobin. *Biochemistry* **47**, 517–525.

27 Milazzo L, Hofbauer S, Howes BD, Gabler T, Furtmüller PG, Obinger C & Smulevich G (2018) Insights into the active site of coproheme decarboxylase from *Listeria monocytogenes*. *Biochemistry* **57**, 2044–2057.

28 Giordano D, Pesce A, Boechi L, Bustamante JP, Caldelli E, Howes BD, Riccio A, di Prisco G, Nardini M, Estrin D *et al.* (2015) Structural flexibility of the heme cavity in the cold-adapted truncated hemoglobin from the Antarctic marine bacterium *Pseudoalteromonas haloplanktis* TAC125. *FEBS J* **282**, 2948–2965.

29 Liu Y, Moenne-Loccoz P, Hildebrand DP, Wilks A, Loehr TM, Mauk AG & Ortiz de Montellano PR (1999) Replacement of the proximal histidine iron ligand by a cysteine or tyrosine converts heme oxygenase to an oxidase. *Biochemistry* **38**, 3733–3743.

30 Eakanunkul S, Lukat-Rodgers GS, Sumithran S, Ghosh A, Rodgers KR, Dawson JH & Wilks A (2005) Characterization of the periplasmic heme-binding protein shut from the heme uptake system of *Shigella dysenteriae*. *Biochemistry* **44**, 13179–13191.

31 Milazzo L, Gabler T, Pühringer D, Jandova Z, Maresch D, Michlits H, Pfanzagl V, Djinović-Carugo K, Oostenbrink C, Furtmüller PG *et al.* (2019) Redox cofactor rotates during its stepwise decarboxylation: molecular mechanism of conversion of coproheme to heme. *ACS Catal* **9**, 6766–6782.

32 Gottfried DS, Peterson ES, Sheikh AG, Wang JQ, Yang M & Friedman JM (1996) Evidence for damped hemoglobin dynamics in a room temperature trehalose glass. *J Phys Chem* **100**, 12034–12042.

33 Peterson ES, Friedman JM, Chien EY & Sligar SG (1998) Functional implications of the proximal hydrogen-bonding network in myoglobin: a resonance Raman and kinetic study of Leu89, Ser92, His97, and F-helix swap mutants. *Biochemistry* **37**, 12301–12319.

34 Hansson M & Hederstedt L (1994) *Bacillus subtilis* HemY is a peripheral membrane protein essential for protoheme IX synthesis which can oxidize coproporphyrinogen III and protoporphyrinogen IX. *J Bacteriol* **176**, 5962–5970.

35 Yang M, Wang Y, Chen Y, Cheng Z, Gu J, Deng J, Bi L, Chen C, Mo R, Wang X *et al.* (2015) Succinylome analysis reveals the involvement of lysine succinylation in metabolism in pathogenic *Mycobacterium tuberculosis*. *Mol Cell Proteomics* **14**, 796–811.

36 Festa RA, McAllister F, Pearce MJ, Mintseris J, Burns KE, Gygi SP & Darwin KH (2010) Prokaryotic ubiquitin-like protein (Pup) proteome of *Mycobacterium tuberculosis* [corrected]. *PLoS One* **5**, e8589.

37 Kuberl A, Polen T & Bott M (2016) The pupylation machinery is involved in iron homeostasis by targeting the iron storage protein ferritin. *Proc Natl Acad Sci USA* **113**, 4806–4811.

38 Alleyn M, Breitzig M, Lockey R & Kolliputi N (2018) The dawn of succinylation: a posttranslational modification. *Am J Physiol Cell Physiol* **314**, C228–C232.

39 Franco R, Al-Karadaghi S & Ferreira GC (2011) Resonance Raman spectroscopic examination of ferrochelatase-induced porphyrin distortion. *J Porphyr Phthalocyanines* **15**, 357–363.

40 Medlock A, Swartz L, Dailey TA, Dailey HA & Lanzilotta WN (2007) Substrate interactions with human ferrochelatase. *Proc Natl Acad Sci USA* **104**, 1789–1793.

41 Hofbauer S, Hagmüller A, Schaffner I, Mlynek G, Krutzler M, Stadlmayr G, Pirker KF, Obinger C, Daims H, Djinović-Carugo K *et al.* (2015) Structure and heme-binding properties of HemQ (chlorite dismutase-like protein) from *Listeria monocytogenes. Arch Biochem Biophys* **574**, 36–48.

42 Deniau C, Gilli R, Izadi-Pruneyre N, Létoffé S, Delepierre M, Wandersman C, Briand C & Lecroisey A (2003) Thermodynamics of heme binding to the HasA (SM) hemophore: effect of mutations at three key residues for heme uptake. *Biochemistry* **42**, 10627–10633.

43 Hofbauer S, Dalla Sega M, Scheiblbrandner S, Jandova Z, Schaffner I, Mlynek G, Djinović-Carugo K, Battistuzzi G, Furtmüller PG, Oostenbrink C *et al.* (2016) Chemistry and molecular dynamics simulations of heme b-HemQ and coproheme-HemQ. *Biochemistry* **55**, 5398–5412.